Peer reviewed version

Link to published version (if available):
10.2514/1.C033909

Link to publication record in Explore Bristol Research
PDF-document

University of Bristol - Explore Bristol Research
General rights

Evaluation of a Compliant Mechanism-Based Droop-Nose Morphing Wingtip via Experimental Tests

Srinivas Vasista[1], Johannes Riemenschneider[2], Bram van de Kamp[3], and Hans Peter Monner[4]
German Aerospace Center (DLR), Braunschweig, 38108, Germany

and

Ronald C. M. Cheung[5], Christopher Wales[6], and Jonathan E. Cooper[7]
University of Bristol, Bristol, BS8 1TH, United Kingdom

A morphing droop-nose wingtip with span of 1.3 m and target 2° droop was designed, manufactured, and tested as part of the European project NOVEMOR. The morphing droop-nose device featured a fiberglass composite skin with optimized 3D thickness distribution which was supported by topology-optimized superelastic nickel titanium and aluminium internal compliant mechanisms. The tests included ground and low speed wind tunnel tests (55 m/s) with the aim of assessing the structural performance and the design chain through measurements of shape, strains, surface pressures, and total forces/moments on the model. Comparisons with the experimental results were used for validation of the computational models and optimization tools. The morphing device was able to change shape whilst resisting the external loads, and it was identified that the distribution of strain and shape accuracy may be improved through the use of a concurrent as opposed to sequential design chain and other developments to the optimization tools. The use of a superelastic material facilitated the high-strain displacement, exceeding 2% strain in the design case and measured up to 4.54%, making it highly suitable for compliant mechanism

---

[1] Postdoctoral Research Engineer, Institute of Composite Structures and Adaptive Systems, Lilienthalplatz 7, Braunschweig 38108, Germany, AIAA member.
[2] Deputy Head of Dept. (Adaptive Systems), Institute of Composite Structures and Adaptive Systems, Lilienthalplatz 7, Braunschweig 38108, Germany.
[3] Research Engineer, Institute of Composite Structures and Adaptive Systems, Lilienthalplatz 7, Braunschweig 38108, Germany.
[4] Professor, Head of Dept. (Adaptive Systems), Institute of Composite Structures and Adaptive Systems, Lilienthalplatz 7, Braunschweig 38108, Germany, AIAA senior member.
[5] Research Assistant, University of Bristol, Bristol, BS8 1TH, United Kingdom
[6] Research Assistant, University of Bristol, Bristol, BS8 1TH, United Kingdom.
[7] RAEng Airbus Sir George White Professor of Aerospace Engineering, Dept. of Aerospace Engineering, Queens Building, AFAIAA.

applications. This paper explains the insights made from the experimental tests and recommendations for the future design of morphing structures.

I. Introduction

MORPHING aircraft structures have been identified as potential enablers for reduced fuel consumption and environmentally friendlier aviation, benefits which are highly sought after by the European Commission and other governing bodies [1–4]. Through morphing devices, an aircraft can adapt its shape to best suit the prevailing conditions, thereby operating at a higher efficiency over the full mission profile. Encompassing a broad definition, morphing has been considered for various applications on a range of aircraft sizes, from small scale UAVs to passenger jetliners to fighter aircraft. For larger aircraft such as passenger jetliners, a more feasible application has been the replacement of leading and trailing edge slats and flaps with morphing devices featuring smooth and gapless skins. In this manner further benefits may be achieved through a more laminar airflow leading to reduced drag as well as reduced airframe noise emissions [5,6,7]. An even further subset of morphing technology is the use of compliant mechanisms as carefully arranged flexible substructures supporting and driving the smooth skin. These mechanisms hold high potential for use in morphing systems given the benefits over conventional sliding/pinned/rigid-link mechanisms of reduced wear, easier assembly, and the elimination of backlash [8–11]. Such compliant mechanisms need to fulfill critical functions and their design is an important step in the morphing system design chain and is crucial to overall system performance.

The research field of morphing aircraft structures has progressed extensively over the last decades with the development of smart materials, novel compliant designs and new multidisciplinary and structural optimization design tools [12–17]. There is a careful trade-off between aerodynamic efficiency, weight, ease of manufacture and assembly, maintainability and cost which determines the overall success of morphing devices. In light of this highly multidisciplinary nature, the benefits can only be assessed from the overall systems level and are dependent on how well the different aspects of design are integrated in the design chain. The effort in morphing technology is continuing as the research community and aeronautical industry draws closer to industrializing the technology through the completion of tasks such as bird-strike testing, fatigue testing, high-speed wind tunnel testing, consideration of lightning protection, anti-icing and de-icing of a morphing droop-nose leading edge device of a

passenger jet [18–21] as well as the completion of flight tests of a passenger jet aircraft with morphing trailing edge flaps [22].

This paper presents the ground and wind tunnel test results of a regional jetliner droop-nose full scale morphing wingtip designed and manufactured as part of the EU FP7 project NOVEMOR (NOvel Air VEhicle Configurations: From Fluttering Wings to MORphing Flight) [23]. The reference geometry, provided by project partner Embraer, is shown in Fig. 1 and features a highly 3D geometry with sweep, taper in chord and thickness directions, multiple curvatures, dihedral, and a streamwise morphing target droop deflection of 2°. The anticipated benefit with this morphing device was an improvement of aeroelastic characteristics, though as per the project aims it was not intended to quantify this anticipated benefit, but to assess the structural design. The wingtip comprised two main assemblies: the droop-nose morphing leading edge and the wingbox/trailing edge assemblies. The droop-nose morphing leading edge featured a flexible and tailored fiberglass skin and internal compliant mechanisms fabricated from superelastic nickel titanium and aluminium alloys. The design of the morphing droop-nose followed a sequential design chain which includes aerodynamic, structural, manufacturing and assembly considerations. The new aspects of work in this design chain include the complete redevelopment of the 2D skin optimization tool used in [5,24] for 3D wing geometries, the development of continuum gradient-based topology optimization with an integrated stiffness-flexibility problem formulation for the design of the compliant mechanism, the various post-processing tools to convert the optimization results into manufacturable formats, as well as novel manufacturing techniques and the use of smart materials. As mentioned, the purpose of the wind tunnel tests was not to quantify the aerodynamic benefits of the morphing device, but to assess the morphing structure under aerodynamic loads. The experimental tests allowed the implementation of the design chain and were used to validate the various optimization tools used in the design. The real value of the experimental tests is that they specifically sought to answer the following questions: i) what was the structural response of the morphing device in the various tests and what physical insights can be made about the final design?; and ii) what do the results mean for the design chain? i.e. as lessons for general morphing design, what needs to be improved in the design chain and how should this be achieved? Measurements of shape from a 3D scanner and strain from strain gauges in the ground tests, and measurements of strain, surface pressures from pressure tappings, and force and moment from the wind tunnel balance in the wind tunnel tests at various flow speeds and angles of attack were used to make the assessments.

This paper first presents a brief background of the design chain and optimization tools. The finite element (FE) model of the complete leading edge morphing device is then presented for the comparison with ground test results. The wind tunnel test methodology and results are then presented in conjunction with the computational fluid dynamics (CFD) analysis. The discussion of the results and ramifications on the design chain are subsequently presented and the conclusions stated.

II. Droop-Nose Morphing Wingtip Design, Manufacture and Assembly

A. Droop-Nose Leading Edge

The design and manufacture of the droop-nose leading edge device is briefly presented here and the reader is referred to [25] for detailed information.

1. Design Chain

A sequential design chain which is based on that of [5,24] was redeveloped to incorporate compliant mechanisms instead of conventional rigid link mechanisms, as shown in Fig. 2. It should be first noted that the structural architecture (Fig. 3a and b) was predefined i.e. the number of compliant mechanisms (2), their locations (equidistant along stringer) and their orientations (perpendicular to spar and bending axis, perpendicular to dihedral) as well as the number of actuators (2). The process is described as follows. After acquiring the target aerodynamic shapes and loads from the aerodynamic optimization (performed by project partners and outside the scope of this paper), the structural design process begins with the design of the skin. An optimization tool generates an optimized three-dimensional thickness distribution over the entire leading edge surface as well as the optimized location for the double-L stringer, such that the outer profile best matches the target droop shape under actuation whilst remaining stiff enough to resist external forces. The optimum thickness distribution that the program finds is physically achieved through using an appropriate number of plies (HexPly® 913) specified by a pre-set stacking sequence "look-up" table. This pre-set table ensures a symmetrical lay-up at every point of the leading edge surface, and the corresponding stacking sequence for each element is incorporated in the finite element analysis. The resulting skin stiffness, resisting forces and internal geometry from the skin optimization stage are transferred to the compliant mechanism design stage. In this process, a topology optimization tool is used to design the compliant mechanisms, which transfer the force from the actuator to the skin with precise displacement and support the skin against the external aerodynamic forces. The results from both stages are then post-processed for the manufacturing stage. It

was assumed in this work that actuation would be provided by linear actuators independently driving each compliant mechanism.

2. Optimization Tools

The skin optimization tool featured a Nelder-Mead Simplex update scheme [26] and 20 design variables (DVs): 16 thickness DVs on the leading edge surface at 21 locations with bilinear interpolation, 2 DVs to represent the stringer position at two spanwise locations, and 2 DVs representing the force magnitudes in the downward direction at the skin-mechanism connection points. The objective function was to minimize the sum of the squared errors between actuated and target displacements for the clean, droop without aerodynamic loads, and droop with aerodynamic loads load cases to account for both the flexibility and stiffness requirements. The compliant mechanisms were designed through continuum gradient-based topology optimization with the "solid isotropic material with penalization" (SIMP) material model [27–30]. A new problem formulation was explored with the objective function being the maximization of stiffness for the clean load case subject to displacement constraints (i.e. morphing shape precision) for the droop load case. Due to the tight space and high resistive force from the skin and aerodynamic loads in the outboard station, the strains were reported in the post-processed finite element analysis as exceeding the material yield strain. The outboard mechanism was modified to overcome this issue and a pin-joint was used at the stringer-mechanism interface.

3. Manufacture

The skin was manufactured from prepreg fiberglass and the 32 plies were cut to the optimized shape and laid up on the mold, vacuum bagged and cured. The skin was completed in two halves and joined together thus involving two curing stages and was necessary given the tight access into the leading edge especially in the tip region. Each half of the skin had tapered layers which would form a lapped connection with sufficient strength once fully cured and the final skin was mounted to the aluminium spar (Fig. 4). The compliant mechanisms were fabricated from wire electrical discharge machining (wire-EDM) of nickel titanium superelastic material (inboard, Fig. 5) and laser cutting of aluminium 7075 (outboard), with an out-of-plane thickness of 5 mm each. The compliant mechanisms were each connected to a linear stepper motor actuator (maximum stroke of 25.4 mm and maximum force of >2 kN at 5 mm/s linear speed) which were mounted onto the spar. The output-ends of the compliant mechanisms were attached to the stringer of the skin. This assembly was then bolted to the wingbox for the wind tunnel tests.

B. Wingbox-Trailing Edge Structure

1. Design

The wingbox was designed within the constraints of cost, manufacturing time and safety requirements. A frame-skin arrangement was used to allow a high-precision surface finish and routing for cables and tubings. The skin consisted of multiple panels for access during assembly and featured an interlocking design to improve safety in case of panel failure during testing. The wingbox was modelled through NASTRAN [31] using a combination of solid elements and bar elements for bolted connections to verify a minimum safety factor of 2.0 would be met under critical loads. The FE model was also extended for flutter clearance.

2. Manufacture

The internal frame was mainly manufactured using standard steel sections, with the root connection to the force platform made from CNC aluminium to facilitate the sweep angle. The skin panels were milled from machineable plastic (ebaboard 140) to ensure a precise surface finish.

C. Assembly and Instrumentation

The leading edge and wingbox frame were initially assembled outside the wind tunnel along with the upper side skin panels. The assembly was then mounted to the force platform before cable and tubing connections were secured. In the final phase of assembly, the lower side skin panels were attached and alumimium tape was used to cover the panel edges.

Measurements in the experimental tests were made through the ATOS Triple Scan [32] device, strain gauges, pressure tappings, and the wind tunnel balance. Further instrumentation included external displacement sensors as a means to check the actuator stroke, and video cameras mounted within the leading edge to obtain real-time visualization of the compliant mechanisms.

A total of 14 bonded strain gauges in a quarter-bridge configuration were used with 6 placed on the inner surface of the skin (designated as {A, BQ, BL, CQ, CL, D}), 6 on the inboard compliant mechanism (designated as {IB1 – IB6}), and 2 on the outboard mechanism (designated as {OB7 – OB8}) as shown in Fig. 6a-c. This type was chosen as total strain (i.e. combined axial and bending strain) was required for comparison with the finite element analysis which featured a very fine mesh with shell elements. The strain gauge signals were first amplified by a calibrated amplifier before being captured by LMS data acquisition hardware and the LMS test.Xpress measurement software [33]. 63 pressure tappings (39 on the leading edge, 24 on the trailing edge) were used in a streamwise orientation at

a station 555 mm from the wind tunnel model root plane as shown in Fig. 7. A photograph of the camera mounted for the inboard compliant mechanism is shown in Fig. 8.

External displacement sensors were installed in an open-loop configuration to provide the current position information of the actuator. Whilst programming of the motors was achieved by specifying a number of steps to deliver the desired actuation stroke, the external displacement sensors were installed in the event that the motor loses steps due to higher than expected loads. It is envisaged for future use to use closed-loop feedback control via the motor encoder. The external displacement sensors were mounted to 3D printed mounts attached to the actuator and the sliding sensor was fitted between blocks on the actuator-compliant mechanism coupling.

III.   Numerical Simulations

A. Finite Element Analysis

The finite element model of the leading edge assembly was based on the finite element file generated in the skin optimization process and was performed using the ANSYS software [34]. The compliant mechanism post-processed CAD file was imported into the existing optimized skin model and meshed with appropriate connectivity to the skin. All elements in the model were meshed with SHELL181 elements and the skin elements had the appropriate cross section fiberglass lay-up and material property data whilst the compliant mechanisms were a uniform 5 mm thickness. The material properties of the inboard nickel titanium superelastic inboard compliant mechanism were approximated as linear and isotropic based on the manufacturer's data specification (Monolitix AG, Switzerland) with elastic modulus of 70 GPa and Poisson's ratio ν of 0.3 (austenite phase). The outboard compliant mechanism material data was also approximated as linear isotropic with a 70 GPa elastic modulus and 0.3 Poisson's ratio. Material data for the aluminium material had been collected in the laboratory with a tensile test machine and the reader is referred to [35] for the data. The displacement results are shown for the leading edge system in Fig. 9a and the von Mises strain contours are shown on the displaced profiles for the inboard and outboard compliant mechanisms in Fig. 9b and c respectively. For comparison with the ground tests, the loading condition for the finite element analysis was 8 and 4 mm actuation input at the actuation points. The rotation degree of freedom in line with the actuator pin was made free and all other remaining degrees of freedom were fixed at these points. The aft edges of the compliant mechanisms were also made fixed, simulating the rigid attachment to the actuator plate. The aft edges of the skin were also fixed to simulate the connection with the spar.

B. Computational Fluid Dynamics Analysis

CFD simulations were carried out using the Tau solver [36,37] with the Spalart-Allmaras turbulence model [38] for the 0% and 100% droop cases to obtain the pressure field over the entire wind tip. The CFD simulations are compared to the pressures and total loads measured experimentally. The 0% droop case was meshed from the surface CAD geometry. For the 100% droop case the mesh was based on 3D scans of the deformed leading edge performed outside the tunnel. The region captured by the scanner is 5 mm from the inboard and 1 mm from the outboard. In constructing the CFD mesh the inboard surface is linearly extrapolated to tunnel wall. The outboard end was left 1mm shorter.

The CFD simulation was performed for the wing in the tunnel working section. The inflow condition was set as uniform flow at 55m/s. At the exit of the working section an exit-pressure outflow condition was used. This was set up so that the pressure in the working section at the reference pressure point matches the measured experimental value.

C. FEA with CFD c_p Distribution and Consideration at Flight Speeds

Following the wind tunnel tests and CFD analysis, the pressure loads obtained from the CFD analysis were imported back into the finite element model. This was done for further confidence in the finite element model which was then ultimately used to assess the device at design flight speeds. As the CFD and finite element meshes were different, a radial basis function 3D scattered data interpolation tool [39,40] was used to map the surface pressures onto the finite element mesh. Two cases were conducted at 0° AoA, 55 m/s and -10° AoA, 55 m/s.

IV.   Testing

A. Ground Tests

The droop-nose leading edge assembly was tested in the laboratory before the wind tunnel tests to check the assembly of all components, and functionality of the control system, mechanisms and sensors. The ground test also served to determine if the device performed in agreement with calculated results. Shape measurements were made through the 3D ATOS scanner in the undeformed and deformed states. The scanner provided full 3D geometric data and from this the profile sections at the inboard and outboard stations were extracted and compared with the finite element analysis results and the target shapes. Strain measurements were made through the strain gauges.

B. Wind Tunnel Tests

After assembling the leading and wingbox/trailing edge parts together, the wingtip was mounted in a vertical orientation in the wind tunnel as shown in Fig. 10**Error! Reference source not found.**a and b. This allowed a wider range of tunnel speeds and angles of attack to be tested compared to the horizontal position because it incorporated the high capacity force platform for measuring the large root bending moments expected at high wind tunnel speed and angle of attack.

The wind tunnel test matrix involved running three different droop configurations (0%, 50% and 100% droop corresponding to 0 / 0 mm, 4 / 2 mm and 8 / 4 mm actuator stroke for inboard / outboard mechanisms respectively) through angles of attack (AoAs) ranging from -10° to +10° at 5° increments and wind tunnel test speeds from 25 to 55 m/s at 5 m/s increments as shown in Table 1. The test matrix needed not be fixed but could evolve based on, for instance, the behaviour of the structure at lower speeds/angles of attack.

The steady state measurements were made once the wind flow had settled at the target air speed. Data collected over these steady state runs were measured over 6 seconds and then averaged. Two transient cases were also conducted at a steady flow speed of 50 m/s and another transient with air-off as shown in Table 2, whereby the data was measured whilst the leading edge was drooping and un-drooping. As there was a large amount of data collected in these tests, for the sake of brevity only the results most relevant to the aims of this paper are presented. At the end of the wind tunnel testing, the inboard compliant mechanism was driven to 250% stroke to investigate the magnitude of allowable deformation of the device.

V.   Results and Discussion

An evaluation on the efficacy of the morphing device and its design and manufture process can be made from the results presented. The inferences made below are grouped according to shape accuracy, strain results, and comparisons with CFD analysis and have ramifications on the process chain and future morphing design.

A. Shape Accuracy

A means of determining the accuracy of profile shapes (i.e. clean, droop, calculated, and measured) was performed by determining the maximum displacement error between the different profiles i.e. taking the maximum perpendicular distance between the profiles. The results in Fig. 11 and Table 3 – 4 show mixed results regarding the accuracy of the morphing device to the target shapes. The shape differences between the droop finite element

analysis and droop experimental results are the lowest (3.39 and 4.72 mm for the inboard and outboard stations respectively). This was expected and the small inaccuracies may be attributed to the necessity of larger tolerances for the assembly process given the highly complex 3D geometries and thus resulting geometric misalignments between the finite element analysis and physical model, as well as the approximation of nickel titanium material properties and draping of the composite plies around the multi-curvature leading edge. It should also be noted that the skin displacement is less than expected whilst the inboard compliant mechanism strains at IB1 and IB6 are higher than expected. This shows that the deformation is more localized to the region of the actuator-mechanism connection, thus there is less-than-expected transfer of the actuator displacement onto the skin.

The discrepancies between the finite element results and target shapes may be due to the fact that the finite element results are those without the aerodynamic load which is in a negative lift orientation at 0° AoA as seen in Fig. 12. It was not expected to see as high a difference between the manufactured undeformed model and the clean target shape (3.51 and 4.82 mm for the inboard and outboard stations respectively). It appears that there was some twisting of the skin in the manufacturing process and this needs to be resolved for future applications. It should be kept in mind that the target displacements were small and as a result the percentage errors with respect to the target displacements appear high. It is not expected that these percentage errors will remain as high for larger target droop displacements, rather remain in the same order of mm error.

B. Strains

The ground test strain readings from the strain gauges are presented in Fig. 13a-c for the skin, inboard compliant mechanism and outboard compliant mechanism respectively, along with the strain results extracted from the finite element analysis. There is a good agreement in the trend of strain between the finite element analysis and measured values in the ground tests shown in Fig. 13, with the exception of the outboard compliant mechanism. The mismatch in strain for the outboard mechanism may be due to the outboard mechanism locally deforming at a point away from the strain gauge. The calculated results underestimated the maximum strain at position IB1 (1.87% strain calculated, 2.28% measured) and as expected, the strains in the inboard compliant mechanism are significantly higher than those of the skin and outboard compliant mechanism, with calculated values of maximum strain in the skin and outboard compliant mechanism being 0.1% and 0.6% respectively. The non-uniformity of the strains shows that deformation is occurring in a local region with respect to the total internal leading edge volume i.e. the inboard

compliant mechanism. A better way of balancing the strain distribution is required in the optimization routines and design chain, leading to reduced concentrations and improved fatigue properties.

The wind tunnel test strain results for the skin position BL and inboard compliant mechanism positions IB1 and IB5 are shown in Fig. 14 - Fig. 16[*]. In these figures, variation in aerodynamic load are represented by changing wind velocity and angle of attack on the x-axis at different droop configurations given by the three different rows. One can then draw comparisons between the strain due to aerodynamic loads and strain due to droop, and this is discussed in Section V. These results are selected for presentation in this paper as they feature the highest strain (BL, IB1) or highest variation in strain due to aerodynamic loads (IB5). The transient strain measurements are shown in Fig. 17 for all strain gauges to provide information as to how the structure responds during the action of drooping and un-drooping with and without aerodynamic loads. The results at 250% inboard stroke are shown in Fig. 18.

The measured wind tunnel test strain results show that the morphing device is able to withstand the wind tunnel loads effectively. The maximum variation of strain due to the wind tunnel aerodynamic loads (with the exception of -10° AoA) seen in Fig. 14 - Fig. 16 is in the order of 0.016% for the skin and 0.085% for the compliant mechanisms. This was expected as the skin was designed for flight speeds, considerably higher than the 55 m/s wind tunnel speed. A significant result occurred at -10° AoA, wherein buckling occurred at position IB5 (Fig. 19) which led to the large variation in strain at position IB5 (Fig. 16). The cause of this was the high local loading due to the leading edge root being in close proximity to the wind tunnel wall and is seen by the high local suction peak in Fig. 20a. This event was indicated by the FEA simulations in Fig. 21 where there is a clear trend of increasing strain for IB5 at -10° AoA. The discrepancy in strain magnitude between FEA and experimental results may be due to the reasons aforementioned, namely a mismatch of strain gauge placement to the corresponding point in the FEA, small variations between CFD surface pressure loads and actual wind tunnel pressures, or other small geometric misalignments. Buckling is not expected for normal operations as the local suction peak was caused by the unique wind tunnel wall scenario, and as no buckling is evident in both the ground tests and FEA calculations with flight design surface pressures (Fig. 22). The results in Fig. 21 in general show a good agreement of the inboard compliant mechanism strains between the finite element results with CFD pressures and the wind tunnel results. The strains due to the design aerodynamic loads in Fig. 22a-c are low, with strains in the cruise configuration being 0.018%, 0.077% and 0.11% for the skin, inboard and outboard locations. There is also a low variation in strain between the

_____

[*]Due to an error in the measurement system, the strain measurement at 50% droop, +10° AoA, 30 m/s was missed and so omitted from the shown results.

droop with and without aerodynamic loads with the exception of the outboard compliant mechanism, and suggests that the system possesses suitable stiffness against external static loads. The strain results of these cases for the inboard compliant mechanism are shown in Fig. 21a-b and compared with the wind tunnel results as discussed in Section V-B. The finite element strain results of the design loads are shown subsequently in Fig. 22a-c

The high strain capability of the superelastic nickel titanium material can be seen through the sustained high values of measured strain in the inboard compliant mechanism. The maximum strain due-to-droop value is 2.28% for the 100% droop configuration at position IB1. Further illustrating the high strain capability is the measurement at 20 mm actuator stroke (250% of the design value) as depicted in Fig. 23. In these photographs, the extreme deformations are noticeable in the region of the actuator-mechanism connection in the top right corners. At this configuration, the maximum recorded strain was 4.54% without structural failure though with localized permanent deformation at strain position IB6 as shown in Fig. 24. These values when compared with the 0.7% yield strain of aluminium 7075 shows the suitability of such a material in morphing applications. However, in future work considerations of the aircraft operating temperature range will be required given the temperature dependence of the martensite-austenite phase transformation essential to the superelastic capability of the material [41–43].

C. Comparison with CFD Analysis

Fig. 20 shows the CFD results compared to the experimental data at 55 m/s. The 0% droop cases generally show fairly good agreement with the experimental data. The 100% droop cases do not show as good agreement with the experimental but match the trend in change in pressure coefficient due to droop. It can be seen that the CFD matches the trend in pressure change due to droop but over predicts the amount.

The results show that for angles of attack from -10° to 0° that increasing the droop increases the suction peak by a small amount. For 5° and 10° angles of attack the trend is reversed and increasing the droop leads to a reduction in the pressure coefficients. The pressure results are consistent with lift results shown in Fig. 12 . For negative angles of attack the magnitude of the lift increases with increasing levels of droop. For positive angles of attack, increasing the amount of droop decreases the lift achieved.

As mentioned, the high suction peak for the -10° case is explained by the leading edge being close to the wind tunnel wall at this angle of attack. The maximum c_p variation at 100% droop at -10° AoA is in the order of 0.16. This value was expected to be small given the small droop target of 2° as specified by project partner Embraer.

To further validate CFD simulations the total lift was compared to the experimental lift, see Fig. 12. The CFD results show a linear change in lift across the angle of attack range. This shows fairly good agreement with the measure lift between -5° to 0°. For angle of attack outside this range the CFD over predicts the magnitude of the lift. The CFD also generally predicts a much smaller change in lift from 0% to 100% droop compared to experiment.

D. Ramifications on the Design Chain

The multifaceted procedure of optimization and design, manufacture, assembly and testing led to a number of lessons learned. As the morphing droop-nose device was largely designed-through-optimization, the device can only perform as well as the effectiveness of the optimization subroutines and the design chain in which they are utilized, and the points described here serve as suggestions for future development of these optimization procedures and chain.

It should be first noted that the overall structural architecture was chosen from concept feasibility and engineering judgement as opposed to any optimization method and a short background of these decisions are described as follows. In this work, it was envisaged from the onset that a single-piece flexible skin would be sufficiently supported and driven by two 2D planar compliant mechanisms. The results of the skin optimization could then be resolved and transferred to the compliant mechanism design stage through these two interface regions. The two mechanisms were spaced equidistant along the stringer and oriented normal to the spar (i.e. the effective "hinge axis" of the skin) and to the dihedral to minimize their out-of-plane bending. The use of 2D planar compliant mechanisms was decided by the capability of the topology optimization tool as it was feasible to develop and apply the method in a 2D environment and obtain realizable solutions (3D topology optimization was deemed too computationally expensive to develop and use in the given project timeframe). The decision for 2D planar compliant mechanisms was also due to the readiness of manufacture through laser cutting, water jet cutting or wire EDM and the concept of 2D planar compliant mechanism would be a progression of conventional aircraft wing rib components to "morphing ribs". The whole design-build-test exercise allowed for the development of these individual optimization tools.

More work is needed to address issues such as the determination of the optimum number of compliant mechanisms and their optimum positions and orientations, optimum number of connection points to the skin (i.e. stringers), and the optimum number, type, placement, and orientation of actuators. The shape accuracy and non-uniformity of strain distribution can be improved through careful consideration of these issues, and this investigation

is being undertaken in other projects, including the Collaborative Research Center SFB880 "Fundamentals of High-Lift for Future Commercial Aircraft" in which a large-span extreme-deformation droop-nose morphing device for a regional transport aircraft is being designed [6]. Possibilities for better structural architectures could be simply using more 2D-designed ribs, sized and spaced sufficiently to account for displacement, stiffness, strength, and buckling requirements. Alternatively, a fully 3D-designed substructure is possible though the question of whether multiple 2D ribs are sufficient or a fully 3D substructure is necessary remains to be answered. In argument of the fully 3D design, the exploration of the full 3D leading edge volume through optimization methods may provide a greater solution space than 2D designs and hence lead to a better structural architecture. From an intuitive point of view, the concept of a thin planar rib is not ideal for compliant mechanisms. As deduced through the simple example of a linear cantilever beam with elastic modulus E, length L, and a rectangular cross section with in-plane height h and out-of-plane breadth b subject to a tip load F, the maximum stress per deflection $\frac{\sigma_{\max}}{\delta_{\max}}$ is equal to $\frac{3Eh}{2L^2}$. This derivation is also provided in [11], with respect to the material yield stress limit. The maximum stress per deflection is dependent on the in-plane height h and is independent of the out-of-plane breadth b. This suggests that stress can be reduced by decreasing the in-plane height whilst maintaining stiffness by increasing the out-of-plane breadth. This type of compliant mechanism is then no longer a thin planar rib and instead is a thin-walled 3D structure in which the deformation is achieved through a plate-bending type. Manufacturing, part count, assembly, material wastage, computational expense, and costs are also factors which would influence the decision to use 2D ribs or 3D substructures and need to be considered. Possible alternative manufacturing solutions are presented later.

A number of comments can be made regarding the skin and topology optimization subroutine methods. The skin optimization tool was developed to handle complex 3D geometries and streamwise target droop profiles whilst rendering realizable solutions. The tool can be readily applied to other morphing design cases with larger deflection. However a further advancement can be made for closer modelling of the manufactured part by including a draping simulation in the 3D lay-up through the ANSYS Advanced Composite Pre-post (ACP) module for example. The continuum gradient-based topology optimization method was developed to prevent the appearance of one-node hinges and account for both stiffness and displacement requirements. The results were manufacturable and the kinematics of the final part are in close agreement with those of the direct optimization result. However, there are a number of challenges associated with the method for future applications with larger droop deflection. The most critical is the issue of non-convergence and excessive distortion of elements for nonlinear cases which is the subject

of a significant research effort [44–47]. This work used linear finite element analysis given the small 2° target droop though nonlinear analysis is essential for large-displacement morphing. Further challenges are the interpretation of grey areas and the structural boundary to which the morphed shape is highly sensitive. Exploration of other problem formulations can also be made. In this work, the objective function of maximizing stiffness for the clean load case subject to target displacement constraints in the droop actuation load case means that the compliant mechanism is designed to be a stiff structure which deforms to precise target points under specific boundary conditions. This deformation is facilitated through the use of a high-strain capable superelastic material. The strain results show an imbalance of the distribution over the different components of the leading edge morphing device, as well as an imbalance in the stiffness-flexibility tradeoff. The strains in the design flight cases show low variation in strain due to the loading, thus the whole system could be made more flexible to enable greater droop deflections and thus greater aerodynamic variation. A strain energy-based objective function may lead to a better balance of stiffness and flexibility and may also implicitly consider actuator size and system weight in the design. As evident, further development of the continuum gradient-based topology optimization method is required and given the ability of this method to generate optimum designs from an essentially 'blank canvas' warrants this development, especially for the design of special compliant mechanisms such as pressurized compliant structures [48–50].

The use of heuristic evolutionary methods such as the load path representation method [9] is also a viable option and may lead to a more integrated design chain in which the skin, compliant mechanism and actuation system are designed concurrently rather than sequentially. The heuristic nature eliminates the need for the calculation of sensitivities which may be difficult to obtain for such morphing problems. Connectivity can also be enforced in such methods thereby preventing the issues of non-convergence/ excessive distortion in nonlinear analysis. The skin optimization tool can be embedded into such a load path representation method and with careful selection of design variables and problem formulation, such as an energy-based objective function and displacement constraints, may result in a tool which determines the optimal structural architecture in the full 3D leading edge space along with detailed topological information. In any case, careful consideration of issues such as the number of design variables, the guarantee of a global optimum, and the computational time needs to be made when selecting the optimization type [51].

As mentioned afore, developments in manufacturing techniques are required. One possible solution is the use of additive layer manufacturing which has undergone significant progress in recent years. The use of this method

would relax geometric design constraints in the optimization routines. The ability to 'print' with smart materials such as nickel titanium for its shape memory and/or superelasticity holds high potential for the improvement of morphing structures and work is already underway in this field [52]. Regardless of the method, the material effects of manufacturing processes must be included in the finite element modelling (e.g. printing direction and its related anisotropy in additive layer manufacturing) in order to achieve a highly integrated and accurate design process.

VI.   Conclusion

A droop-nose morphing wingtip was successfully designed, manufactured and experimentally tested as part of the NOVEMOR project aims. The fabricated model was able to change shape whilst subjected to external wind tunnel loads, thereby validating the design tools and chain as being capable of producing realizable morphing devices. The finite element modelling had reasonable agreement with the experimental tests and shows that the design under its design flight loads should also be able to fulfill the morphing requirements adequately. It was not intended to quantify the aerodynamic benefits of the device and certainly further aerodynamic and aeroelastic testing will be required to ascertain the magnitude of the effect of 2° target droop deflection on the flying performance. Nonetheless, it was found that a concurrent design chain is required instead of a sequential one, thereby achieving a higher level of integration between the components. This should lead to a better strain distribution and, in conjunction with a modified problem formulation to consider strain energy as a structural objective, may lead to a better balance of stiffness-flexibility. Comparative studies between 2D and 3D designs are also required. A computationally efficient method is required, as the number of design variables will be significantly higher, especially in 3D cases. Advances in manufacturing technologies such as additive layer manufacturing will be required to fully exploit the advantages of topology optimization results and superelastic materials, though the processing effects must be accounted for in the computational models. The experimental campaign provided a number of insights into the final design and several recommendations for the future design of larger-displacement morphing structures.

References

[1]   "European Aviation Environmental Report 2016" Available: http://ec.europa.eu/transport/modes/air/aviation-strategy/documents/european-aviation-environmental-report-2016-72dpi.pdf. Accessed: February 22, 2016 DOI: 10.2822/385503.

[2]   European Commission, "Flightpath 2050: Europe's Vision for Aviation" Available: http://ec.europa.eu/transport/modes/air/doc/flightpath2050.pdf. Accessed: February 22, 2016 DOI: 10.2777/50266.

[3]   CORDIS, "FP7: Transport (Including Aeronautics)" Available: http://cordis.europa.eu/fp7/transport/. Accessed: February 22, 2016.

[4]   Collier, F., Thomas, R., Burley, C., Nickol, C., Lee, C.-M., and Tong, M., "Environmentally Responsible Aviation - Real Solutions for Environmental Challenges Facing Aviation," *27th Congress of the International Council of the Aeronautical Sciences 2010, ICAS 2010*, 2010.

[5]   Kintscher, M., Wiedemann, M., Monner, H. P., Heintze, O., and Kühn, T., "Design of a Smart Leading Edge Device for Low Speed Wind Tunnel Tests in the European Project SADE," *International Journal of Structural Integrity*, Vol. 2, No. 4, 2011, pp. 383–405, DOI: 10.1108/17579861111183911.

[6]   Burnazzi, M., and Radespiel, R., "Design and Analysis of a Droop Nose for Coanda Flap Applications," *Journal of Aircraft*, Vol. 51, No. 5, 2014, pp. 1567–1579, DOI: 10.2514/1.C032434.

[7]   Sodja, J., Martinez, M. J., Simpson, J. C., and De Breuker, R., "Experimental Evaluation of the Morphing Leading Edge Concept," *23rd AIAA/AHS Adaptive Structures Conference (SciTech 2014)*, January 5-9, AIAA Paper 2015-0791, 2015, DOI: 10.2514/6.2015-0791.

[8]   Lu, K.-J., and Kota, S., "Design of Compliant Mechanisms for Morphing Structural Shapes," *Journal of Intelligent Material Systems and Structures*, Vol. 14, No. June, 2003, DOI: 10.1177/104538903035563.

[9]   Lu, K.-J., and Kota, S., "An Effective Method of Synthesizing Compliant Adaptive Structures Using Load Path Representation," *Journal of Intelligent Material Systems and Structures*, Vol. 16, No. 4, 2005, pp. 307–317, DOI: 10.1177/1045389X05050104.

[10]   De Gaspari, A., and Ricci, S., "A Two-Level Approach for the Optimal Design of Morphing Wings Based On Compliant Structures," *Journal of Intelligent Material Systems and Structures*, Vol. 22, No. 10, 2011, pp. 1091–1111, DOI: 10.1177/1045389X11409081.

[11]   Howell, L., *Compliant Mechanisms*, John Wiley and Sons, New York, 2001.

[12]   Ajaj, R. M., Beaverstock, C. S., and Friswell, M. I., "Morphing Aircraft: The Need for a New Design Philosophy," *Aerospace Science and Technology*, Vol. 49, 2015, pp. 154–166, DOI: 10.1016/j.ast.2015.11.039.

[13]   Weisshaar, T. A., "Morphing Aircraft Systems: Historical Perspectives and Future Challenges," *Journal of Aircraft*, Vol. 50, No. 2, 2013, pp. 337–353, DOI: 10.2514/1.C031456.

[14]   Vasista, S., Tong, L., and Wong, K. C., "Realization of Morphing Wings: A Multidisciplinary Challenge," *Journal of Aircraft*, Vol. 49, No. 1, 2012, pp. 11–28, DOI: 10.2514/1.C031060.

[15]   Barbarino, S., Bilgen, O., Ajaj, R. M., Friswell, M. I., and Inman, D. J., "A Review of Morphing Aircraft," *Journal of Intelligent Material Systems and Structures*, Vol. 22, No. 9, 2011, pp. 823–877, DOI: 10.1177/1045389X11414084.

[16]   Sofla, A. Y. N., Meguid, S. a., Tan, K. T., and Yeo, W. K., "Shape Morphing of Aircraft Wing: Status and Challenges," *Materials & Design*, Vol. 31, No. 3, 2010, pp. 1284–1292, DOI: 10.1016/j.matdes.2009.09.011.

[17]   Thill, C., Etches, J., Bond, I., Potter, K., and Weaver, P., "Morphing Skins," *Aeronautical Journal*, Vol. 112, No. 1129, 2008, pp. 117–139.

[18]   Chary, C., "Development and Validation of a Bird Strike Protection System for an Enhanced Adaptive Droop Nose," *Smart Intelligent Aircraft Structures (SARISTU): Proceedings of the Final Project Conference*, edited by P.C. Wölcken and M. Papadopoulos, Springer International Publishing, Switzerland, 2016, pp. 71–83, DOI: 10.1007/978-3-319-22413-8_3.

[19]   Snop, V., and Horak, V., "Testing Overview of the EADN Samples," *Smart Intelligent Aircraft Structures (SARISTU): Proceedings of the Final Project Conference*, edited by P.C. Wölcken and M. Papadopoulos, Springer International Publishing, Switzerland, 2016, pp. 85–96, DOI: 10.1007/978-3-319-22413-8_4.

[20]   Heintze, O., Steeger, S., Falken, A., and Heckmann, J., "Enhanced Adaptive Droop Nose—from Computer Model to Multi-Functional Integrated Part," *Smart Intelligent Aircraft Structures (SARISTU): Proceedings*

of the Final Project Conference, edited by P.C. Wölcken and M. Papadopoulos, Springer International Publishing, Switzerland, 2016, pp. 97–111, DOI: 10.1007/978-3-319-22413-8_5.

[21]   Kintscher, M., Kirn, J., Storm, S., and Peter, F., "Assessment of the SARISTU Enhanced Adaptive Droop Nose," *Smart Intelligent Aircraft Structures (SARISTU): Proceedings of the Final Project Conference*, edited by P.C. Wölcken and M. Papadopoulos, Springer International Publishing, Switzerland, 2016, pp. 113–140, DOI: 10.1007/978-3-319-22413-8_6.

[22]   Kota, S., Flick, P., and Collier, F. S., "Flight Testing of FlexFloil TM Adaptive Compliant Trailing Edge," *54th AIAA Aerospace Sciences Meeting (SciTech 2016)*, January 4-8, AIAA Paper 2016-0036, San Diego, California, 2016, DOI: 10.2514/6.2016-0036.

[23]   Suleman, A., Vale, J. L., Afonso, F., Lau, F. P., Ricci, S., De Gaspari, A., Riccobene, L., Cavagna, L., Cooper, J., Wales, C., Cheung, R. C. M., Nangia, R., Rizzi, A., Monner, H. P., van de Kamp, B., Vasista, S., Morelli, M., Parizi, J., Odaguil, F., De Lima, G. R., and Antunes, A., "Novel Air Vehicle Configurations: From Fluttering Wings to Morphing Flight," *World Congress on Computational Mechanics (WCCM XI)*, July 20-25, Barcelona, Spain, 2014.

[24]   Rudenko, A., Monner, H. P., and Rose, M., "A Process Chain for Structural Optimization of a Smart Droop Nose for an Active Blown High Lift System," *22nd AIAA/ASME/AHS Adaptive Structures Conference (SciTech 2014)*, January 13-17, AIAA Paper 2014-1414, National Harbor, Maryland, 2014, DOI: 10.2514/6.2014-1414.

[25]   Vasista, S., De Gaspari, A., Ricci, S., Riemenschneider, J., Monner, H. P., and van de Kamp, B., "Compliant Structures-Based Wing and Wingtip Morphing Devices," *Aircraft Engineering and Aerospace Technology*, Vol. 88, No. 2, 2016, DOI: 10.1108/AEAT-02-2015-0067.

[26]   Lagarias, J. C., Reeds, J. A., Wright, M. H., and Wright, P. E., "Convergence Properties of the Nelder--Mead Simplex Method in Low Dimensions," *SIAM Journal on Optimization*, Vol. 9, No. 1, 1998, pp. 112–147, DOI: 10.1137/S1052623496303470.

[27]   Zhou, M., and Rozvany, G. I. N., "The COC Algorithm, Part II: Topological, Geometrical and Generalized Shape Optimization," *Computer Methods in Applied Mechanics and Engineering*, Vol. 89, No. 1-3, 1991, pp. 309–336, DOI: 10.1016/0045-7825(91)90046-9.

[28]   Bendsøe, M. P., "Optimal Shape Design as a Material Distribution Problem," *Structural Optimization*, Vol.

1, No. 4, 1989, pp. 193–202, DOI: 10.1007/BF01650949.

[29]   Mlejnek, H. P., "Some Aspects of the Genesis of Structures," *Structural Optimization*, Vol. 5, No. 1-2, 1992, pp. 64–69, DOI: 10.1007/BF01744697.

[30]   Bendsøe, M. P., and Sigmund, O., *Topology Optimization - Theory, Methods and Applications*, Springer-Verlag, Berlin-Heidelberg, 2003.

[31]   MSC Software Corporation, *MSC NASTRAN*, Software Package, Newport Beach, California, United States, 2015.

[32]   GOM   GmbH,   "ATOS   Triple   Scan   -   Revolutionary   Scanning   Technique"   Available: http://www.gom.com/metrology-systems/system-overview/atos-triple-scan.html.   Accessed: February   22, 2016.

[33]   Siemens PLM Software, *LMS Test.Xpress*, Software Package, Plano, Texas, United States, 2013.

[34]   ANSYS, *ANSYS Mechanical APDL Structural Analysis Guide*, Software Package, Ver. 16, Canonsburg, Virginia, United States, 2014.

[35]   Vasista, S., Riemenschneider, J., and Monner, H. P., "Design and Testing of a Compliant Mechanism-Based Demonstrator for a Droop-Nose Morphing Device," *23rd AIAA/AHS Adaptive Structures Conference (SciTech 2015)*, January 5-9, AIAA Paper 2015-1049, Kissimmee, Florida, 2015.

[36]   Gerhold, T., Galle, M., Friedrich, O., and Evans, J., "Calculation of Complex Three-Dimensional Configurations Employing the DLR-Tau-Code," *35th Aerospace Sciences Meeting and Exhibit*, January 6-9, AIAA Paper 97-0167, Reno, Nevada, 1997, DOI: 10.2514/6.1997-167.

[37]   Galle, M., Gerhold, T., and Evans, J., "Parallel Computation of Turbulent Flows around Complex Geometries on Hybrid Grids with the DLR-TAU Code," *Parallel Computational Fluid Dynamics - Towards Teraflops, Optimization and Novel Formulations*, D. Keyes, A. Ecer, J. Periaux, N. Satofuka, and P. Fox, eds., Elsevier Science, Amsterdam, The Netherlands, 2000.

[38]   Allmaras, S. R., Johnson, F. T., and Spalart, P. R., "Modifications and Clarifications for the Implementation of the Spalart-Allmaras Turbulence Model," *Seventh International Conference on Computational Fluid Dynamics (ICCFD7)*, Paper ICCDF7-1902, July 9-13, Big Island, Hawaii, 2012.

[39]   Buhmann, M. D., *Radial Basis Functions: Theory and Implementation*, Cambridge University Press, Cambridge, United Kingdom, 2003.

[40] Wendland, H., *Scattered Data Approximation*, Cambridge University Press, Cambridge, United Kingdom, 2005.

[41] Zarinejad, M., and Liu, Y., "Dependence of Transformation Temperatures of NiTi-Based Shape-Memory Alloys on the Number and Concentration of Valence Electrons," *Advanced Functional Materials*, Vol. 18, No. 18, 2008, pp. 2789–2794, DOI: 10.1002/adfm.200701423.

[42] Padula, S., Bigelow, G., Noebe, R., Gaydosh, D., and Garg, A., "Challenges and Progress in the Development of High-Temperature Shape Memory Alloys Based on NiTiX Compositions for High-Force Actuator Applications," *International Conference on Shape Memory and Superelastic Technologies, no. 20110001638*, 2006, pp. 1–9, DOI: 10.1361/cp2006smst787.

[43] Hartl, D. J., and Lagoudas, D. C., "Aerospace Applications of Shape Memory Alloys," *Proceedings of the Institution of Mechanical Engineers Part G Journal of Aerospace Engineering*, Vol. 221, No. 4, 2007, pp. 535–552, DOI: 10.1243/09544100JAERO211.

[44] Buhl, T., Pedersen, C., and Sigmund, O., "Stiffness Design of Geometrically Nonlinear Structures Using Topology Optimization," *Structural and Multidisciplinary Optimization*, Vol. 19, 2000, pp. 93–104, DOI: 10.1007/s001580050089.

[45] Pedersen, C. B. W., Buhl, T., and Sigmund, O., "Topology Synthesis of Large-Displacement Compliant Mechanisms," *International Journal for Numerical Methods in Engineering*, Vol. 50, No. 12, 2001, pp. 2683–2705, DOI: 10.1002/nme.148.

[46] Kawamoto, A., "Stabilization of Geometrically Nonlinear Topology Optimization by the Levenberg-Marquardt Method," *Structural and Multidisciplinary Optimization*, Vol. 37, No. 4, 2009, pp. 429–433, DOI: 10.1007/s00158-008-0236-5.

[47] Luo, Q., and Tong, L., "An Algorithm for Eradicating the Effects of Void Elements on Structural Topology Optimization for Nonlinear Compliance," *Structural and Multidisciplinary Optimization*, 2015, DOI: 10.1007/s00158-015-1325-x.

[48] Vasista, S., and Tong, L., "Design and Testing of Pressurized Cellular Planar Morphing Structures," *AIAA Journal*, Vol. 50, No. 6, 2012, pp. 1328–1338.

[49] Vos, R., Barrett, R., and Romkes, A., "Mechanics of Pressure-Adaptive Honeycomb," *Journal of Intelligent Material Systems and Structures*, Vol. 22, No. 10, 2011, pp. 1041–1055, DOI: 10.1177/1045389X11412638.

[50]   Gramüller, B., Boblenz, J., and Hühne, C., "PACS—Realization of an Adaptive Concept Using Pressure Actuated Cellular Structures," *Smart Materials and Structures*, Vol. 23, No. 11, 2014, p. 115006, DOI: 10.1088/0964-1726/23/11/115006.

[51]   Sigmund, O., "On the Usefulness of Non-Gradient Approaches in Topology Optimization," *Structural and Multidisciplinary Optimization*, Vol. 43, No. 5, 2011, pp. 589–596, DOI: 10.1007/s00158-011-0638-7.

[52]   Haberland, C., Elahinia, M., Walker, J. M., Meier, H., and Frenzel, J., "On the Development of High Quality NiTi Shape Memory and Pseudoelastic Parts by Additive Manufacturing," *Smart Materials and Structures*, Vol. 23, No. 10, 2014, p. 104002, DOI: 10.1088/0964-1726/23/10/104002.

Figures:

a) NOVEMOR reference aircraft.
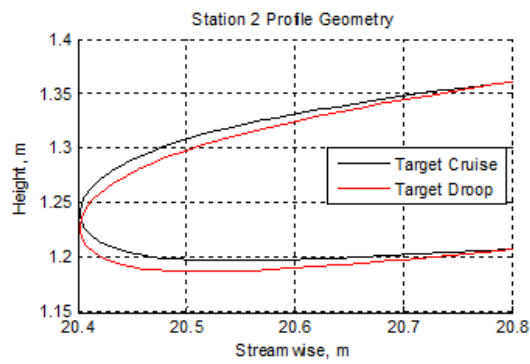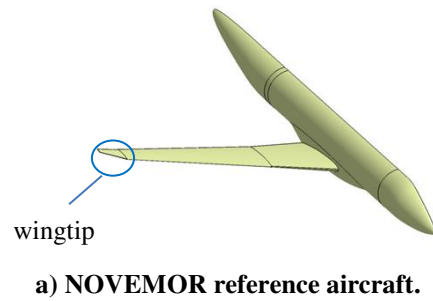
b) Cruise and droop profiles for station 2.
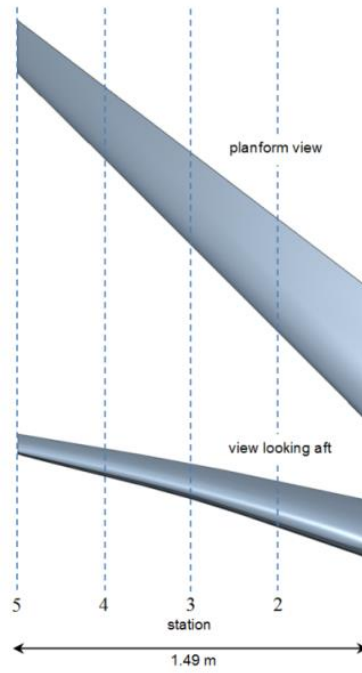
c) Leading edge of wingtip.

Fig. 1 NOVEMOR reference aircraft geometry and detailed wingtip geometry.
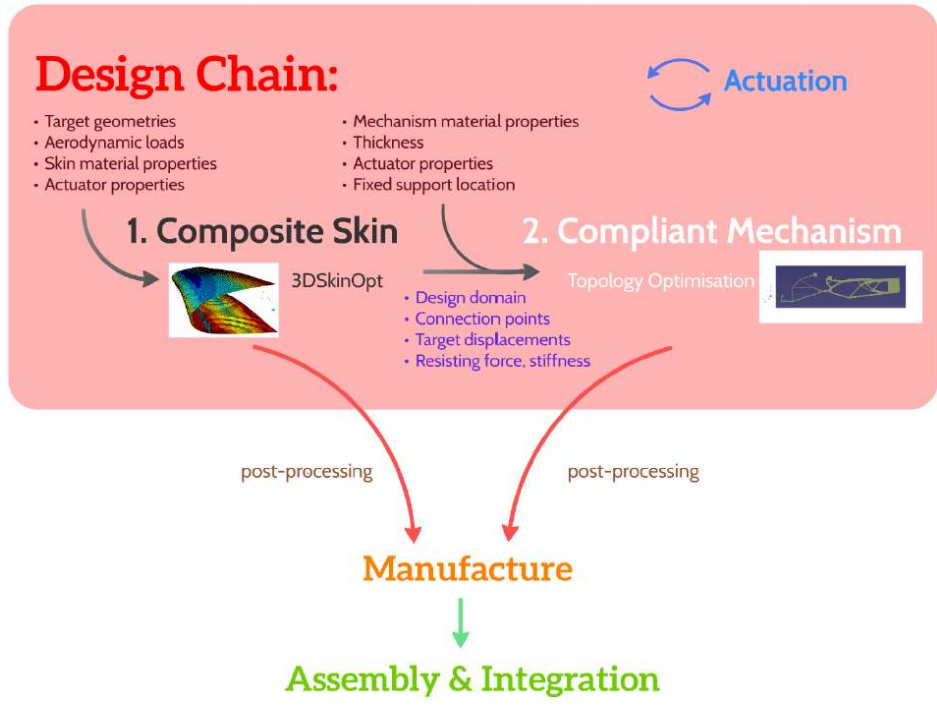
Fig. 2 Design chain for the droop-nose morphing device.
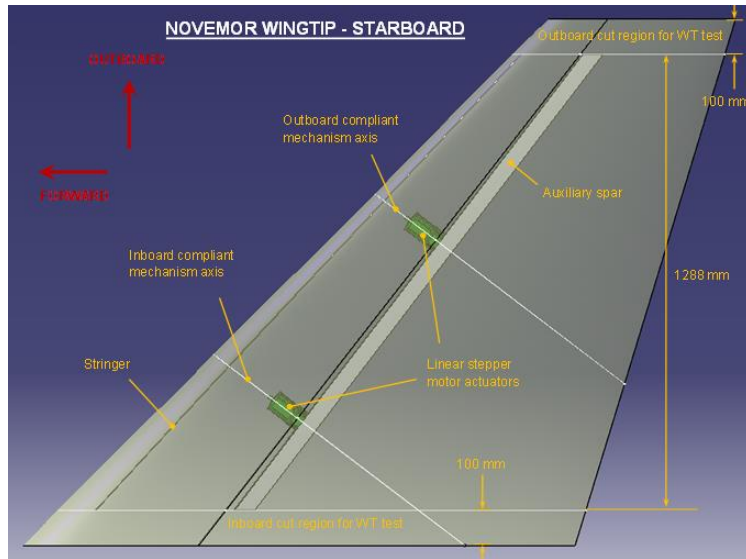
a) Layout of the structural system.
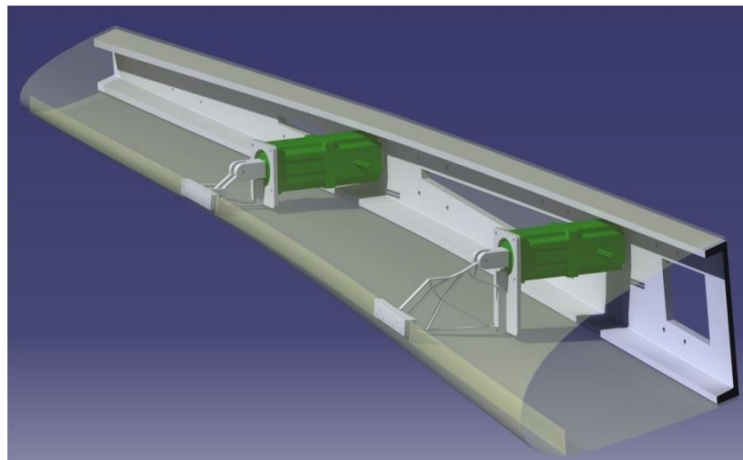
b) Conceptual illustration of the morphing leading edge.

Fig. 3 Morphing leading edge concept.
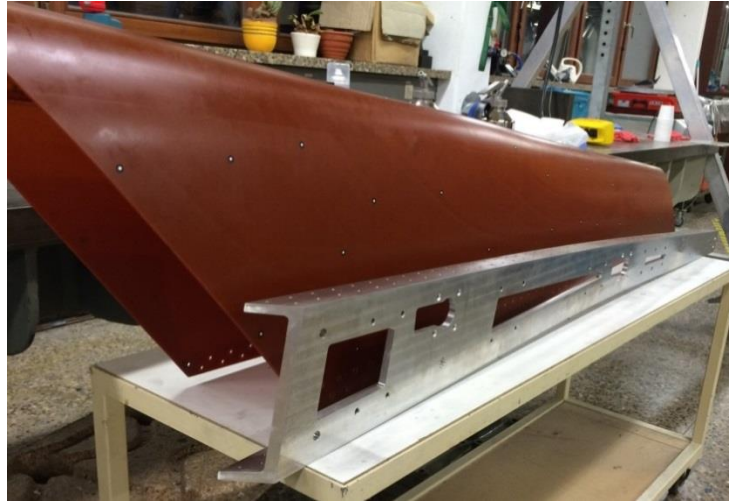
Fig. 4 Manufacturing skin alongside milled aluminium spar.
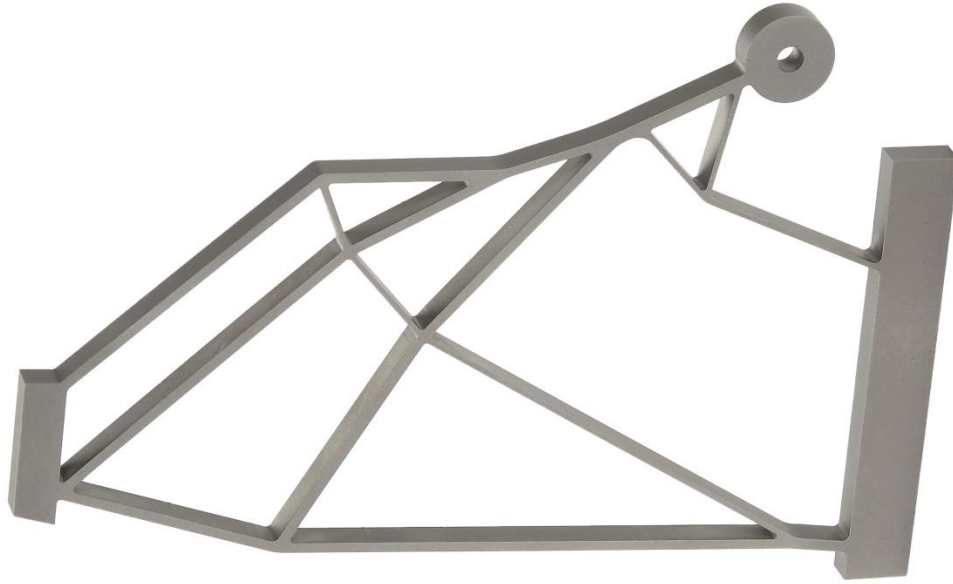
Fig. 5 Photograph of wire EDM-fabricated superelastic nickel titanium inboard compliant mechanism.
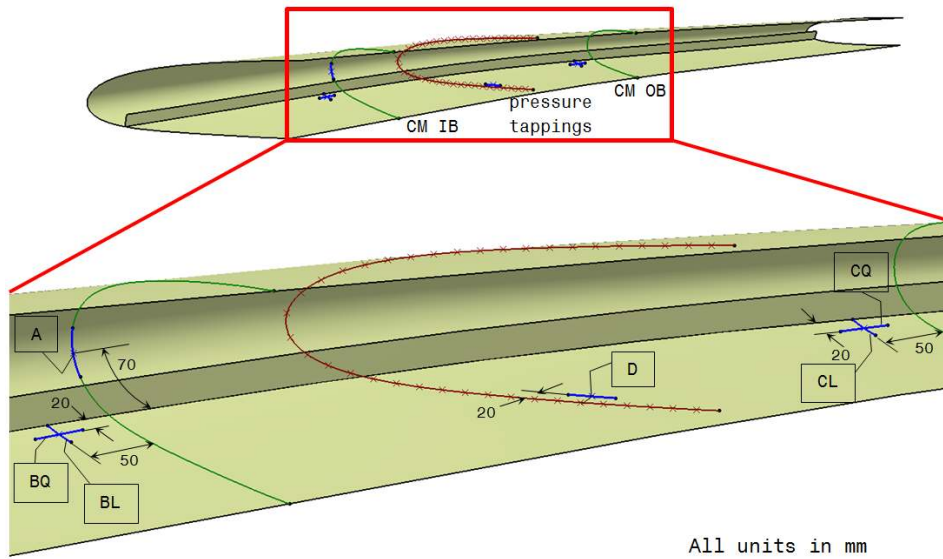
a) Positions on the skin.
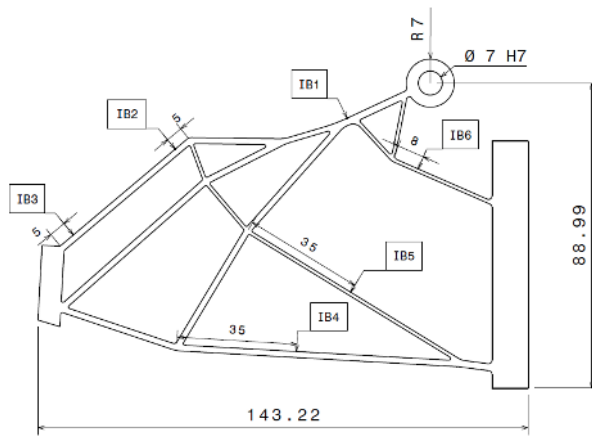
b) Superelastic inboard compliant mechanism.
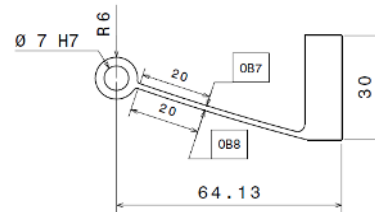
c) Aluminium outboard compliant mechanism.

Fig. 6 Strain gauge locations of the components.
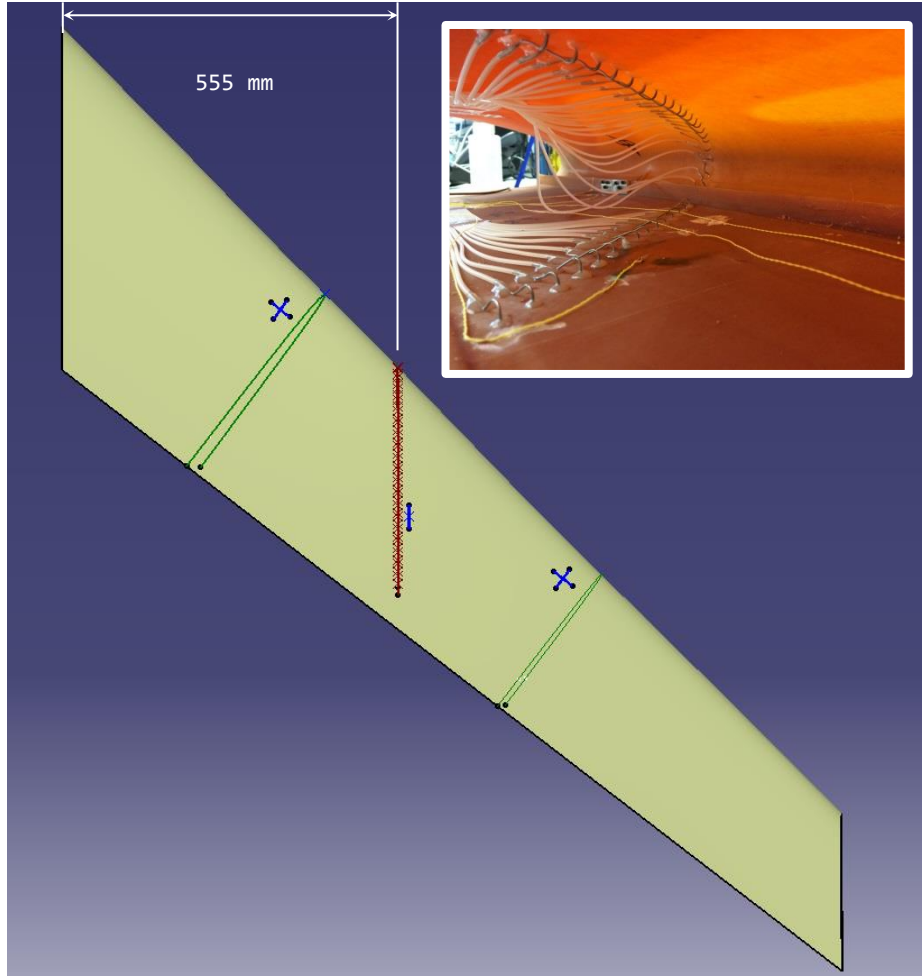
Fig. 7 Schematic of pressure tappings on the leading edge.
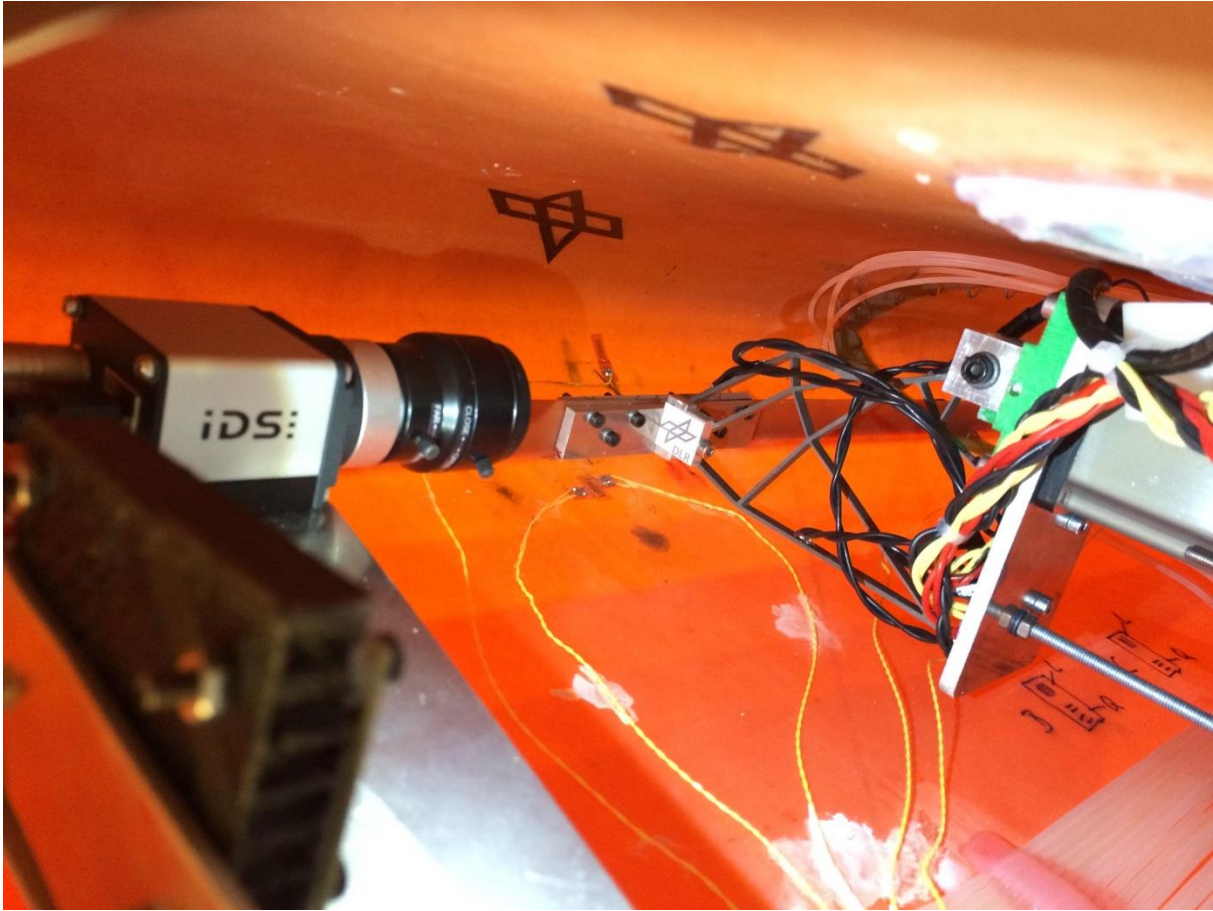
Fig. 8 Photograph of installed inboard compliant mechanism with internal video camera.
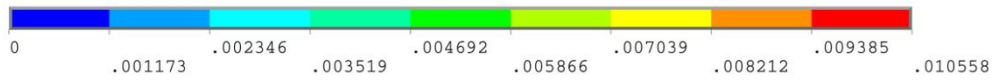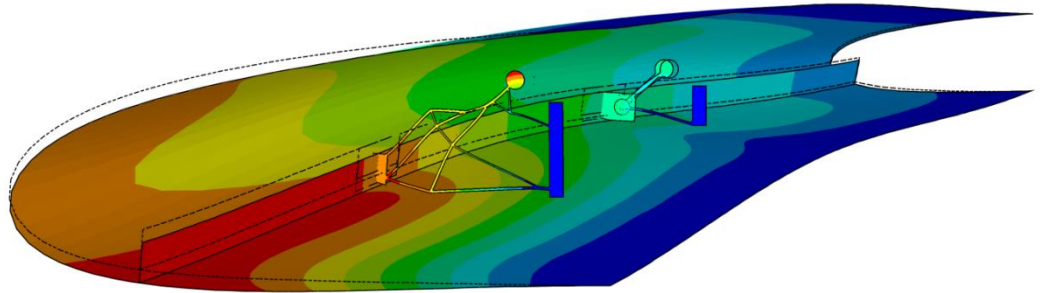
a) Total displacement in meters.
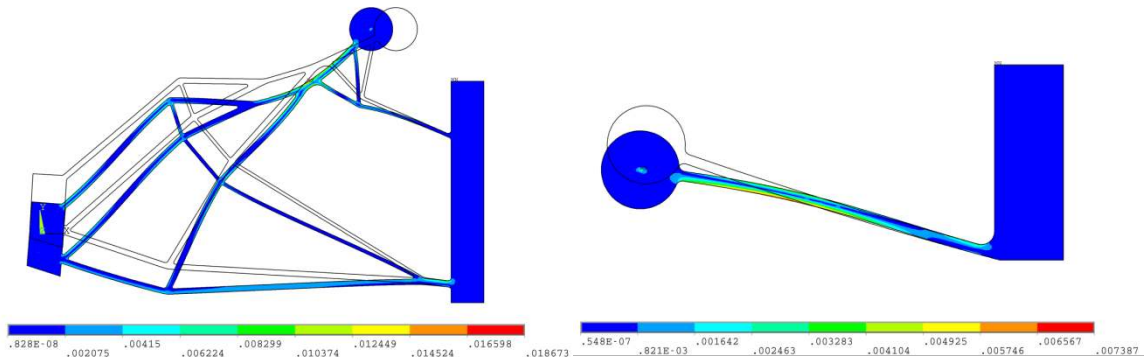
b) Inboard compliant mechanism
von Mises strain field.

c) Outboard compliant mechanism
von Mises strain field.

Fig. 9 Finite element analysis results without aerodynamic loading and 100% droop.
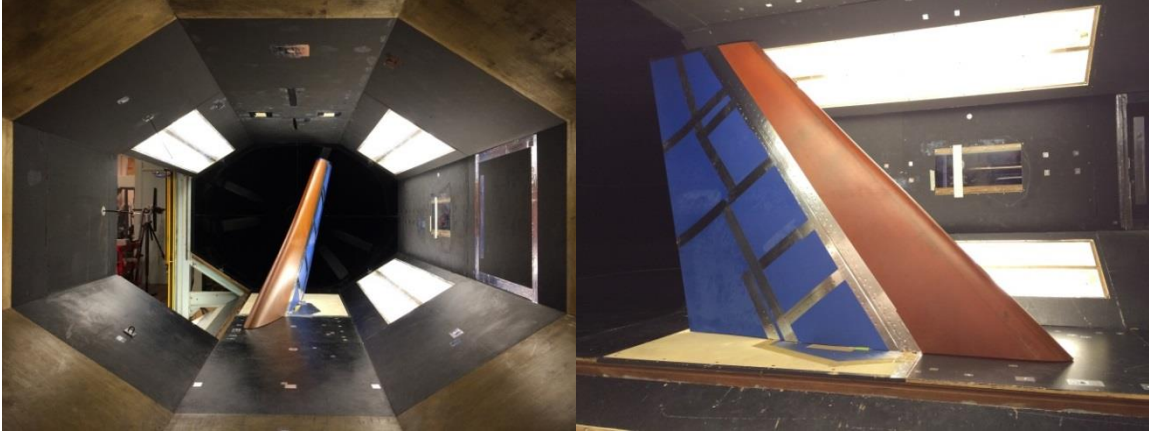
Fig. 10 a) Front and b) side view of the morphing wingtip in the wind tunnel.
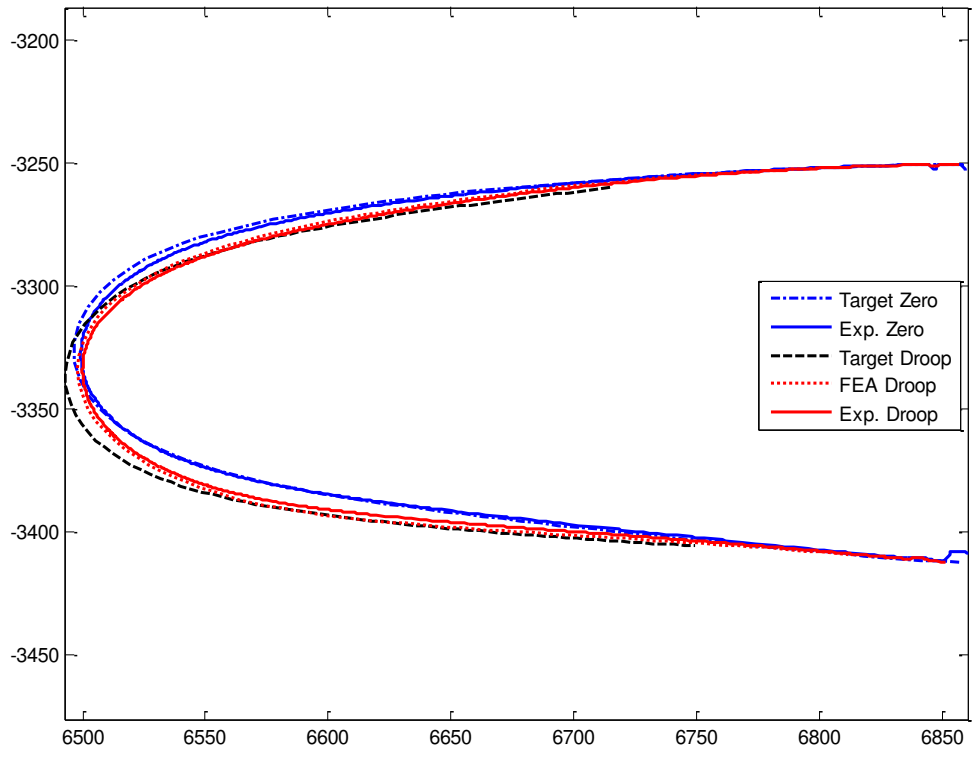
a) Inboard station.
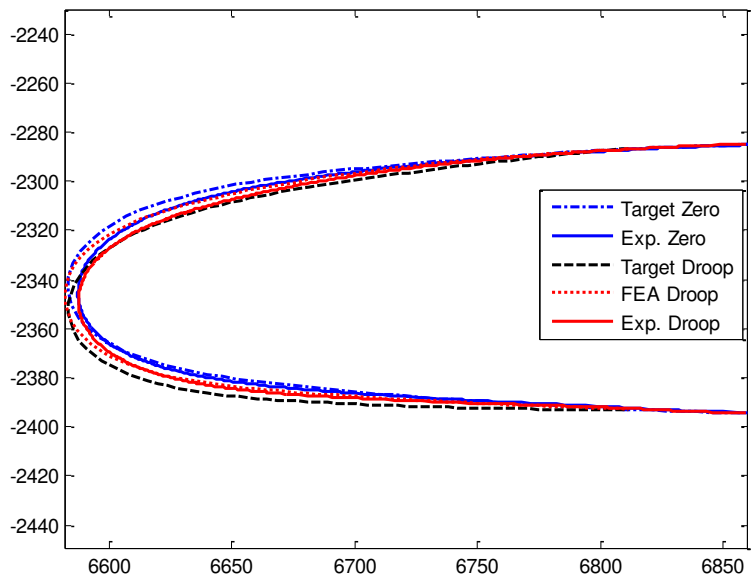
b) Outboard station.

Fig. 11 Comparison between target, calculated and ATOS-measured profile shapes.
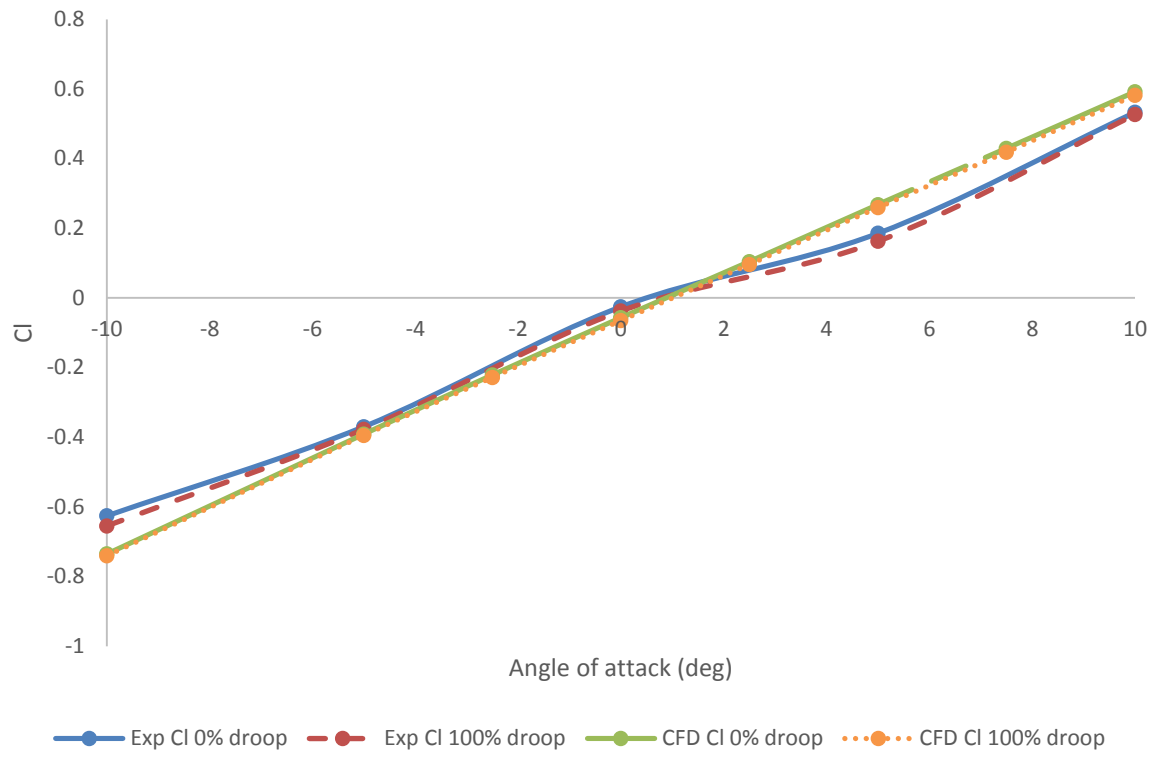
Fig. 12 Comparison of experimental and CFD lift coefficients at 55m/s.
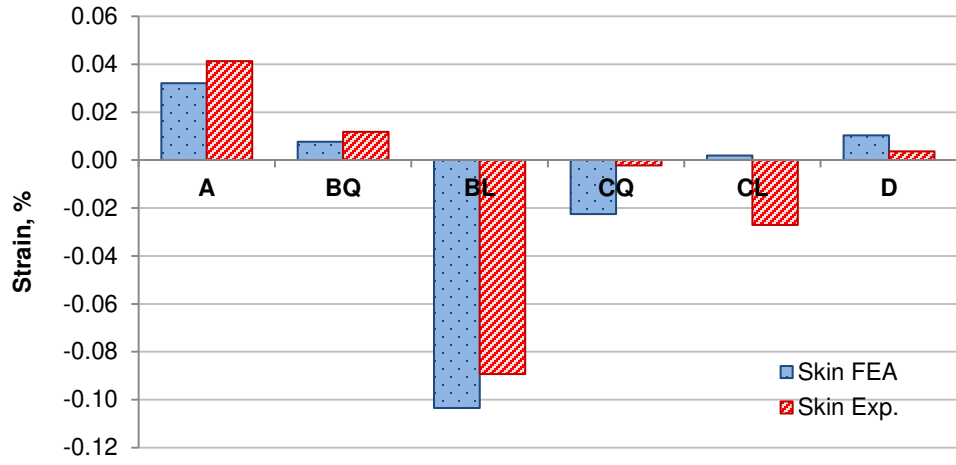
a) Skin results.

b) Inboard compliant mechanism results.
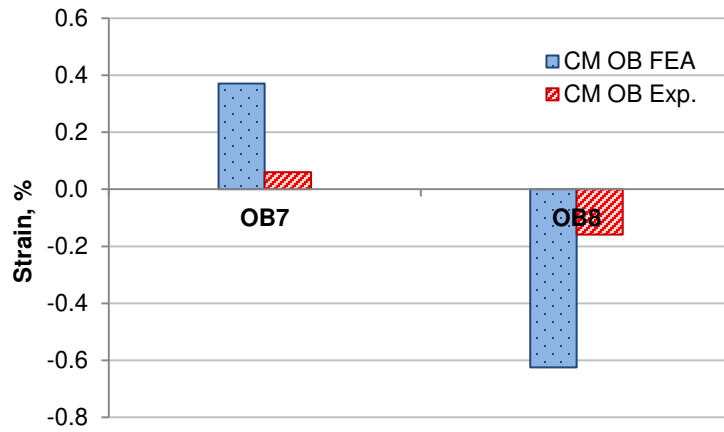
c) Outboard compliant mechanism results.

Fig. 13 Strain comparisons between finite element analyses and experimental ground test measurements.
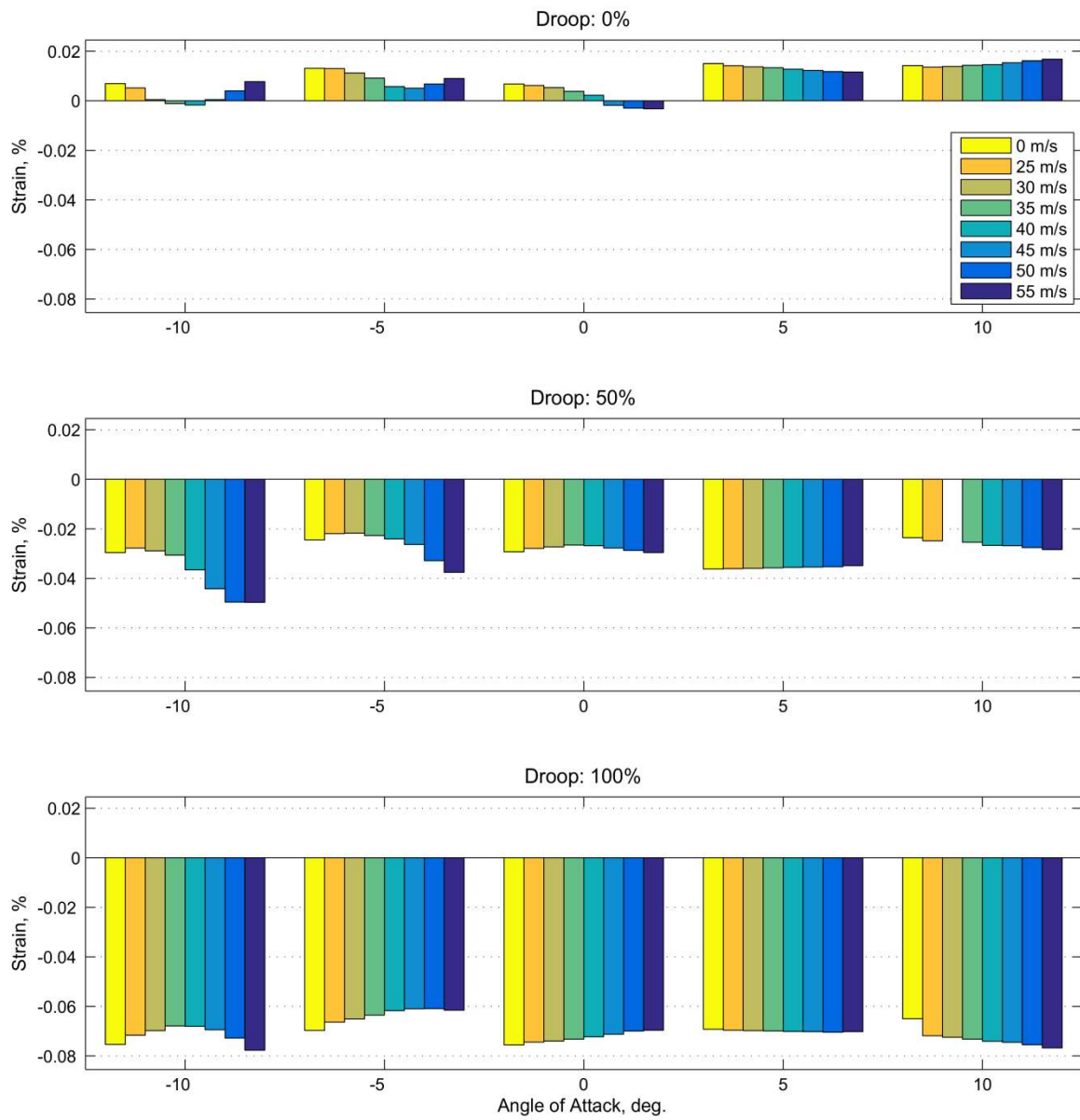
Fig. 14 Strain gauge measurement results at skin position BL in steady-state wind tunnel tests.
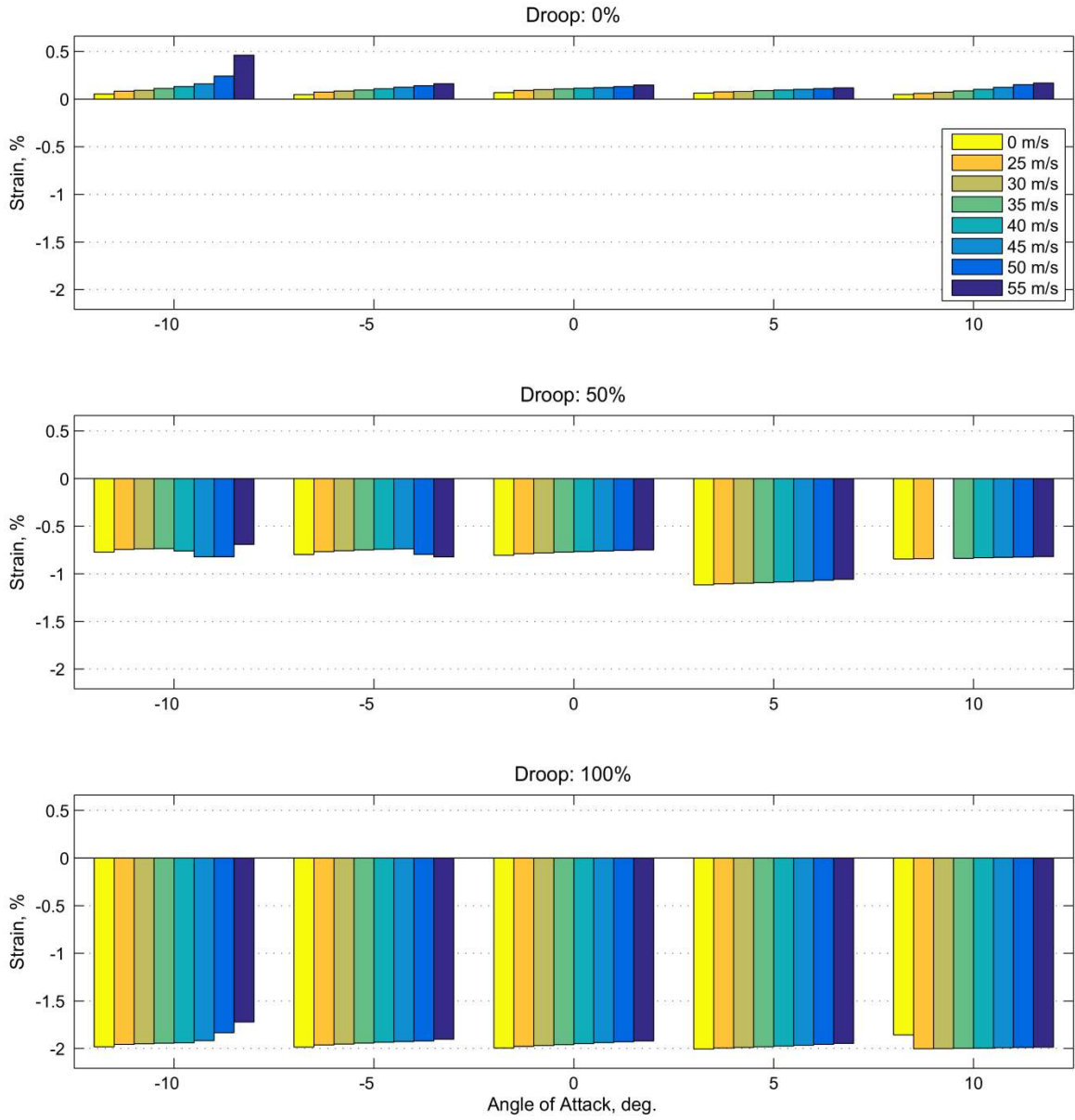
Fig. 15 Strain gauge measurement results at inboard compliant mechanism position IB1 in steady-state wind tunnel tests.
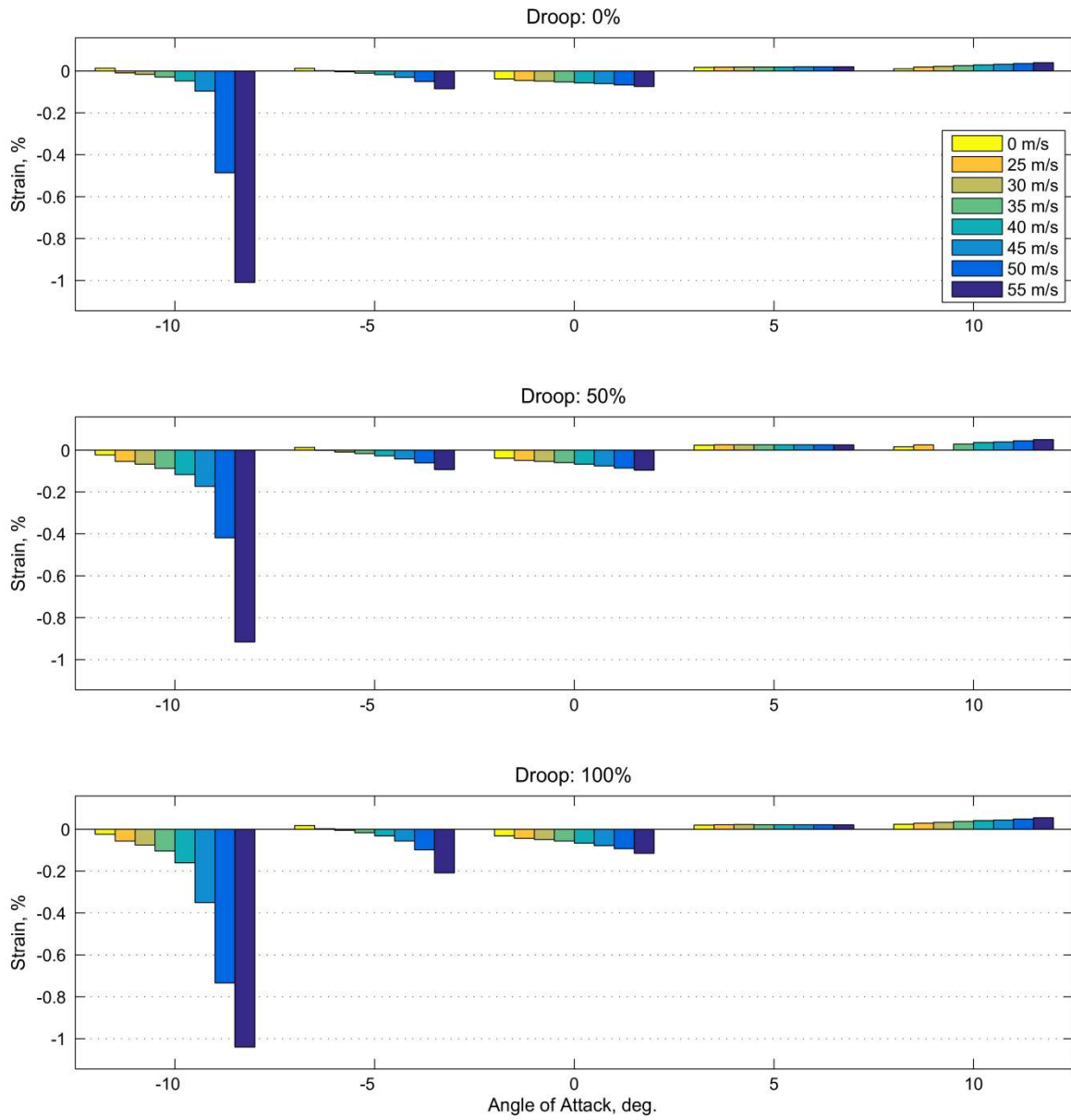
Fig. 16 Strain gauge measurement results at inboard compliant mechanism position IB5 in steady-state wind tunnel tests.
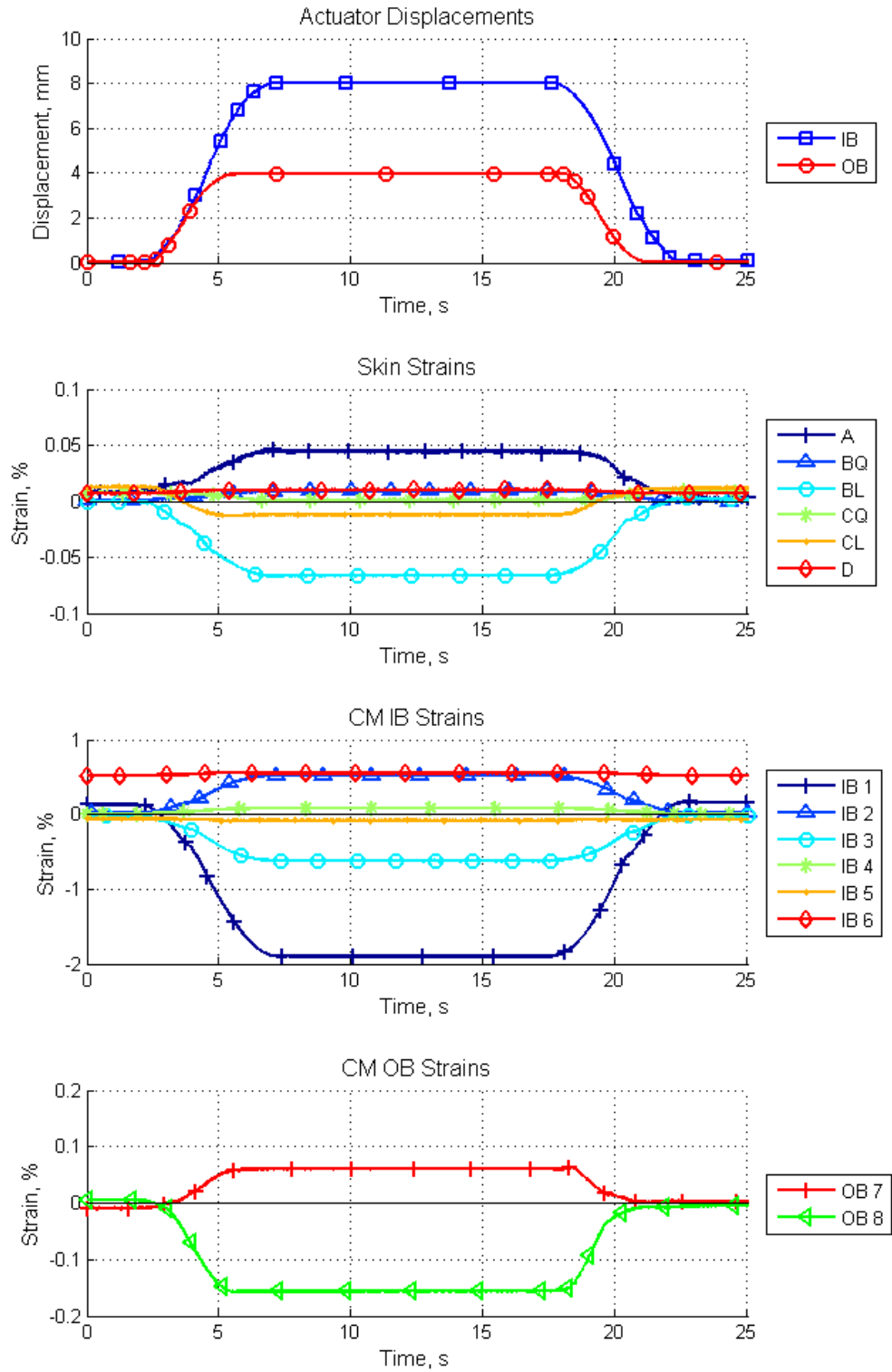
Fig. 17 Transient strain results at 100% droop and 50 m/s flow speed.
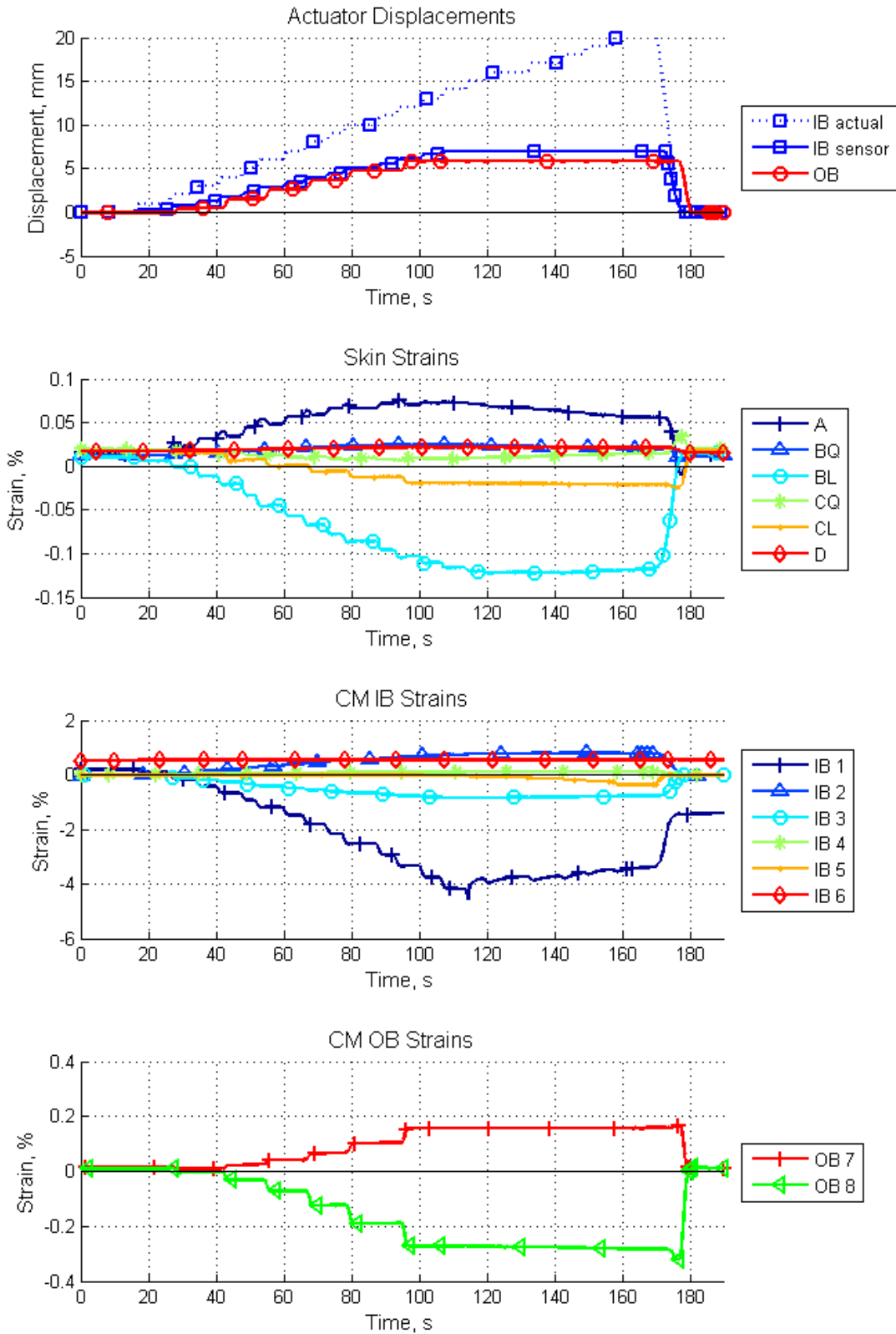
Fig. 18 Transient strain results with inboard actuator stroke of 250% and without airflow.
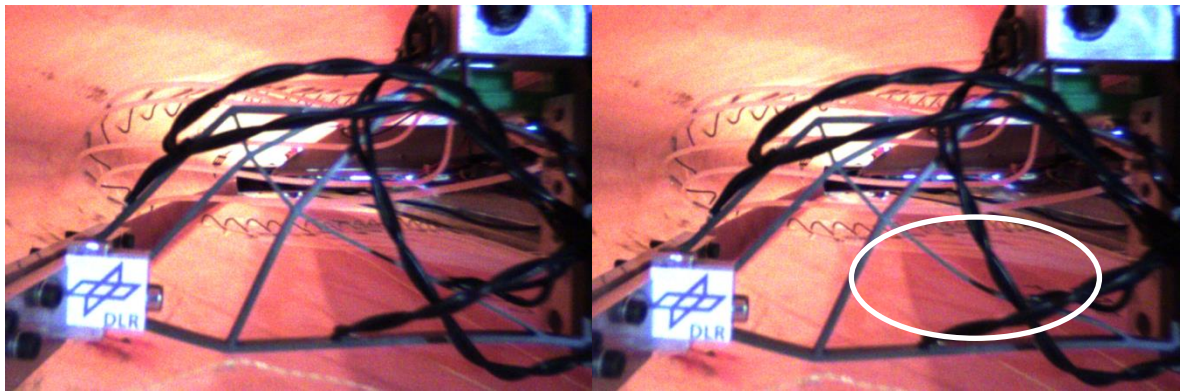
a) 100% droop, zero airflow

b) 100% droop, -10° AoA, 55 m/s
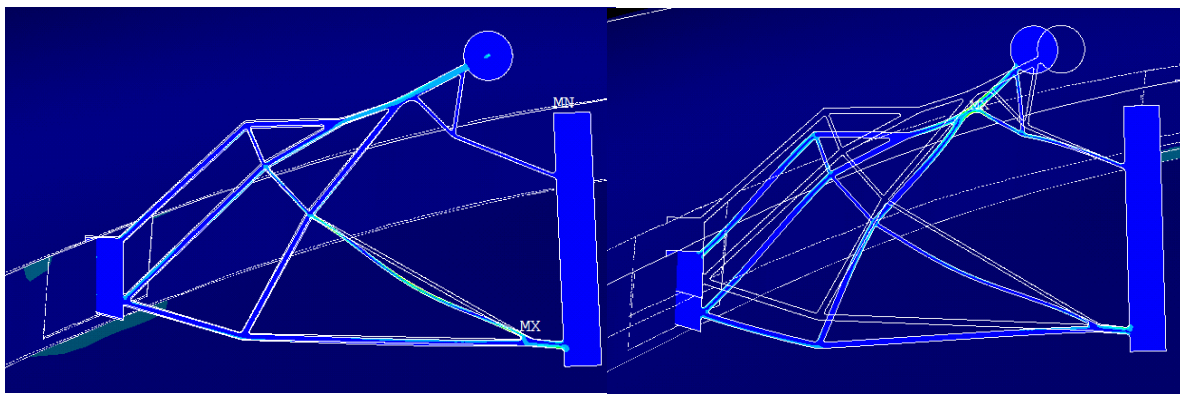
c) Zero droop, -10° AoA, 55 m/s

d) 100% droop, -10° AoA, 55 m/s

Fig. 19 Photographs of inboard compliant mechanism without a) and with buckling b), and finite element analysis showing buckling in c) and d).
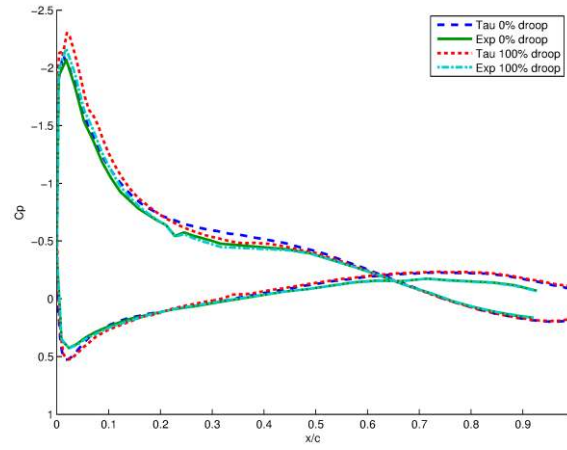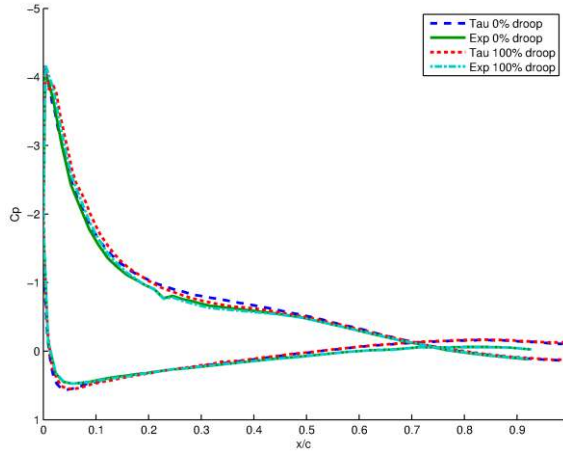
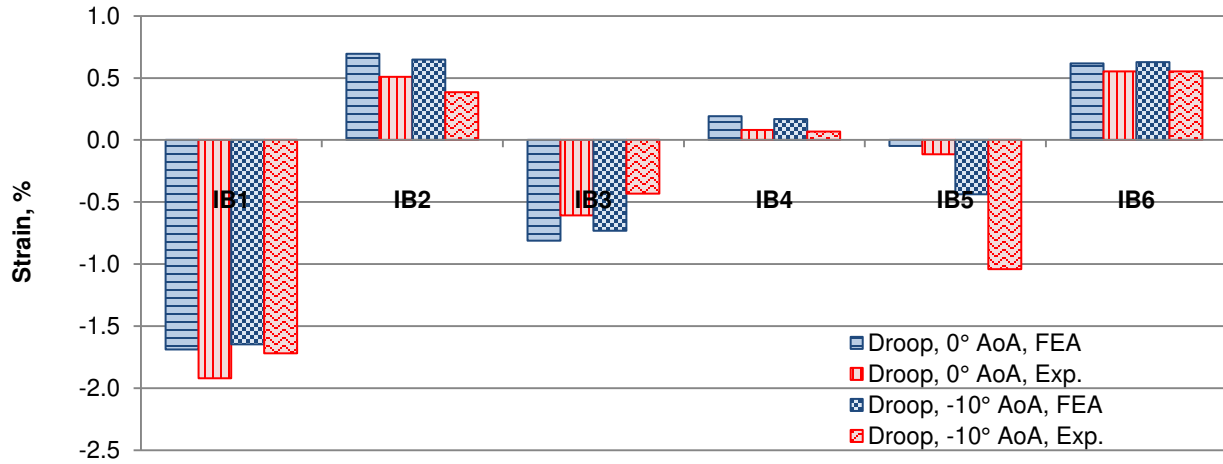a) -10°   b) -5°
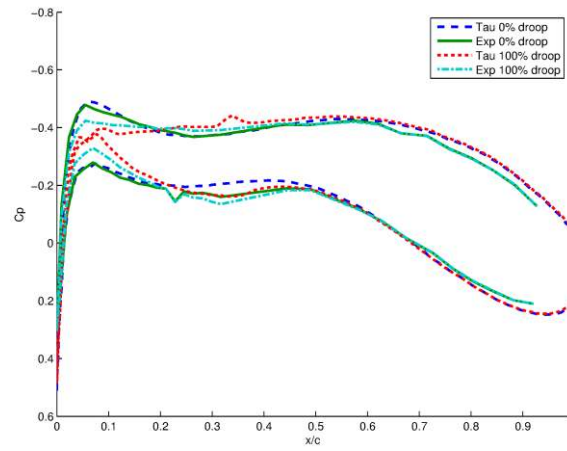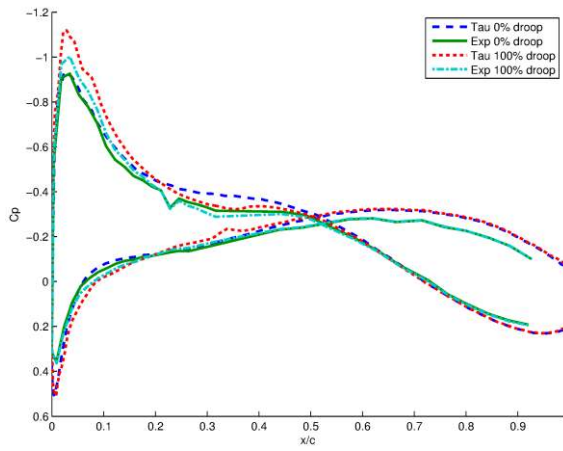
c) 0°   d) 5°
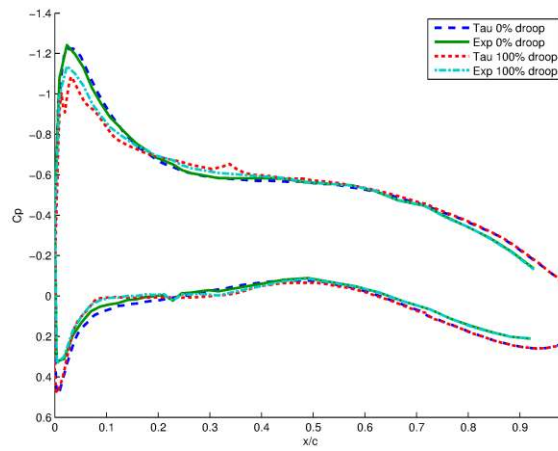
e) 10°

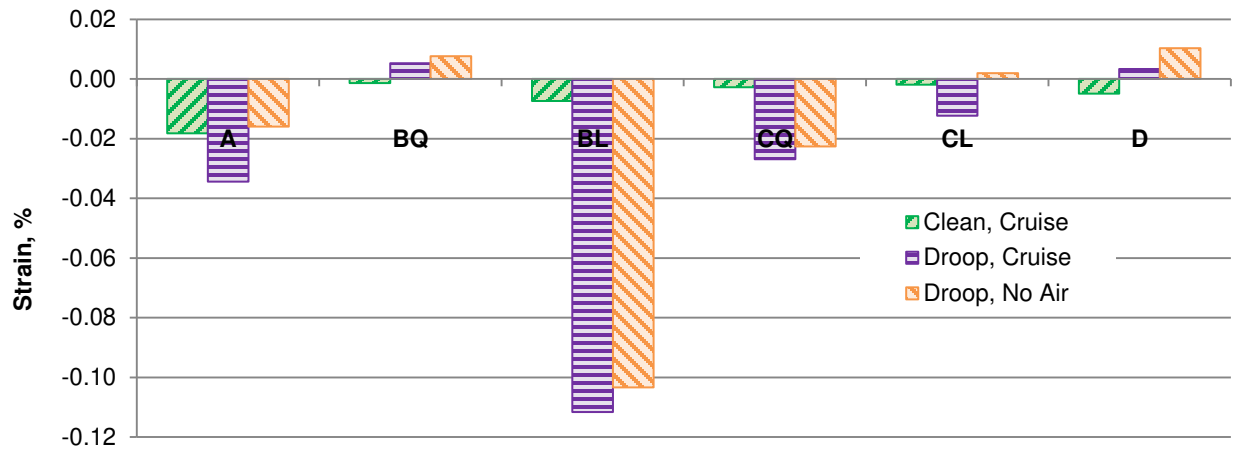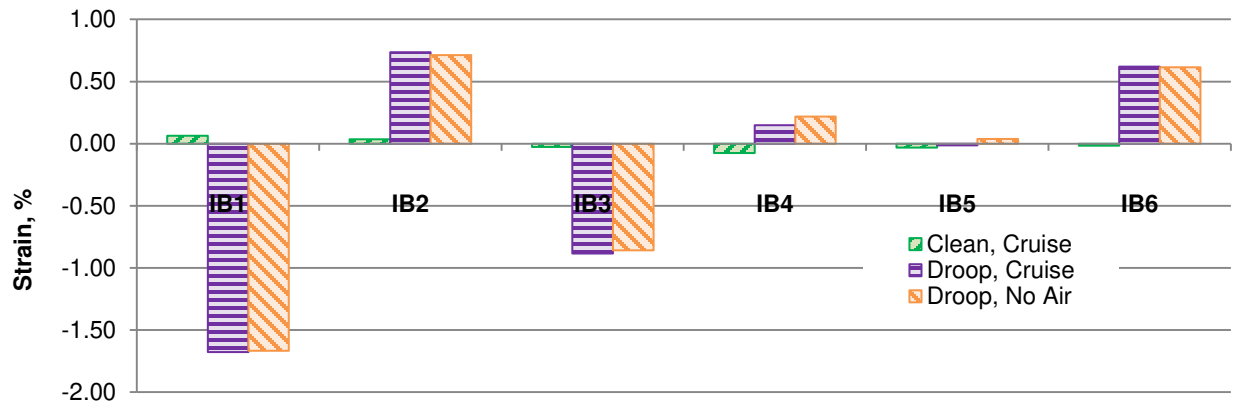**Fig. 20 Comparison of CFD pressures with experimental values at 55m/s**

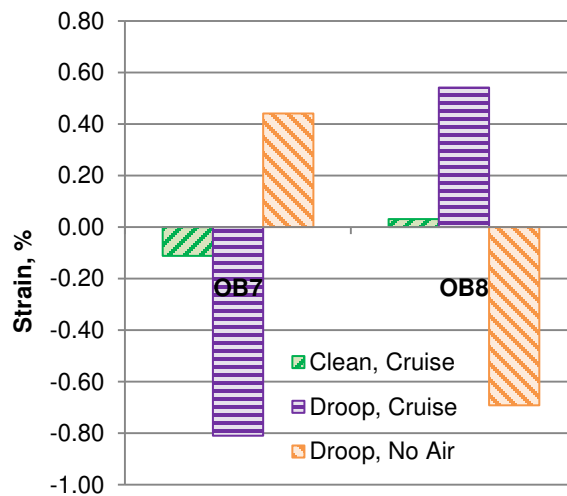**a) Clean case results.**

b) Droop case results.

Fig. 21 Comparison of finite element analysis (with CFD-calculated pressures) and wind tunnel experiment results for the inboard compliant mechanism.

a) Skin results.

b) Inboard compliant mechanism results.

c) Outboard compliant mechanism results.

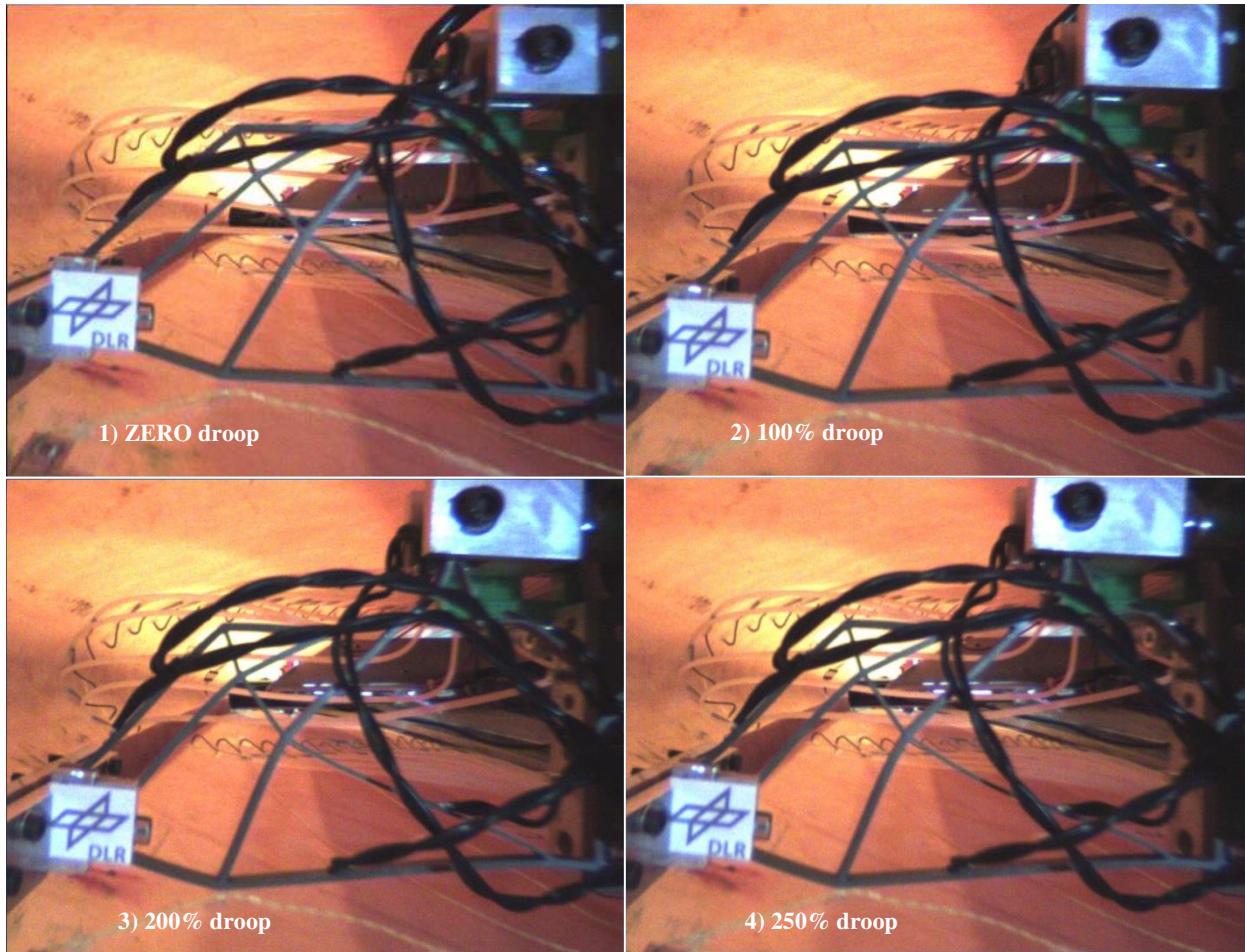Fig. 22 Finite element results of strain with the design cruise pressures.

Fig. 23 Photograph sequence of the inboard compliant mechanism without aerodynamic loading and cycling up to 250% actuator stroke.
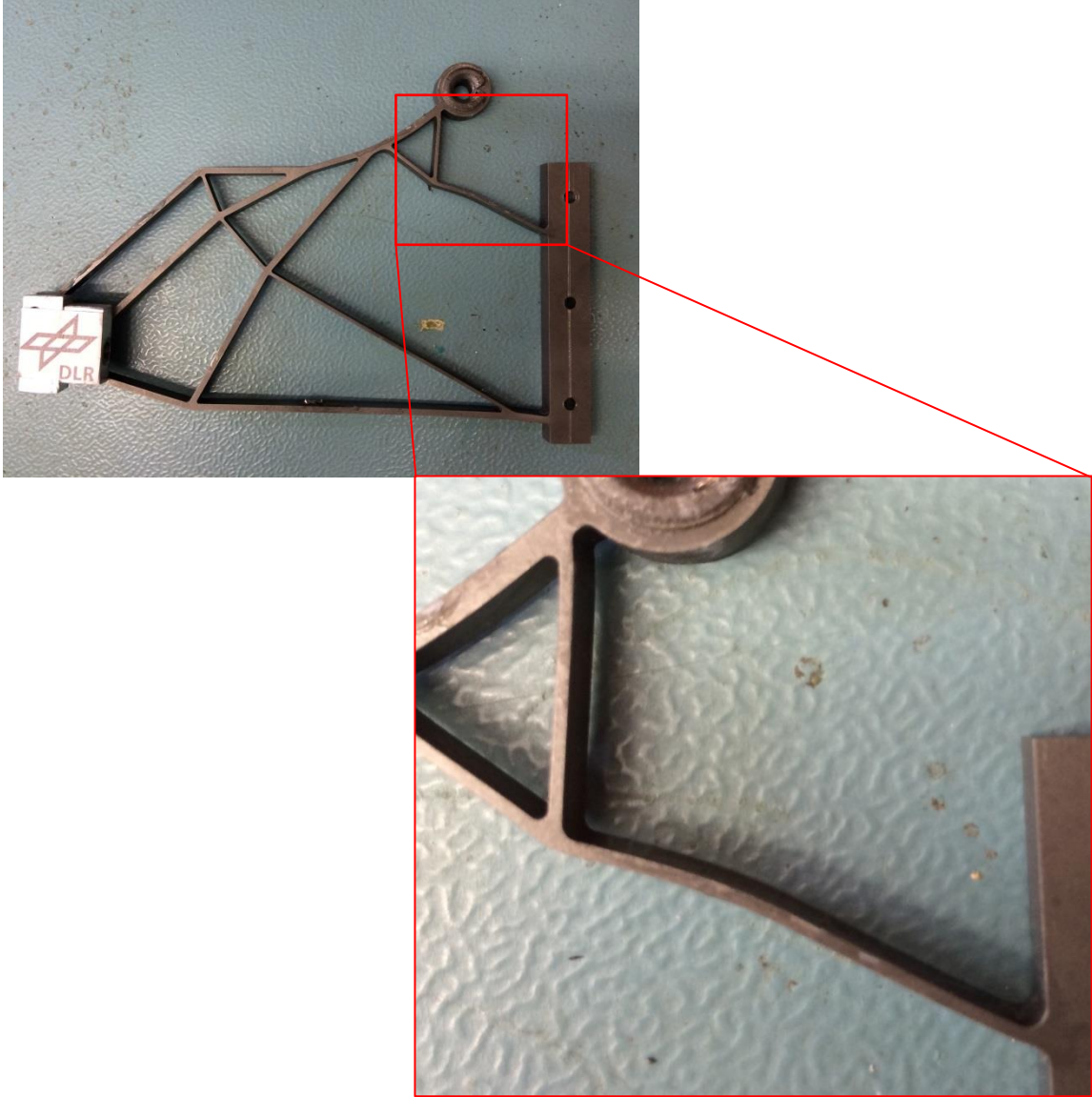
Fig. 24 Inboard compliant mechanism after disassembly with zoomed in region of plastic deformation.

Tables:

Table 1 Test matrix for steady-state measurements.

AoA, °	-10 → +10 @ 5° increments
Droop, %	0, 50, 100
Wind Speed, m/s	0, 25 → 55 @ 5 m/s increments

Table 2 Test matrix for transient measurements. (†inboard compliant mechanism value, outboard stroke was 100%.)

AoA, °	0	0	0
Droop, %	0 → 100 → 0	0 → 200† → 0	0 → 250† → 0
Wind Speed, m/s	50	50	0

Table 3 Errors in profile shape for the inboard station as measured in the ATOS-scans.

Comparison	Maximum Displacement Error, mm
Manufactured undeformed	3.51
Droop FEA – Droop Target	7.60
Droop Exp. – Droop FEA	3.39
Droop Exp. – Droop Target	7.44
Droop Target – Clean Target	10.95

Table 4 Errors in profile shape for the outboard station as measured in the ATOS-scans.

Comparison	Maximum Displacement Error, mm
Manufactured undeformed	4.82
Droop FEA – Droop Target	4.82
Droop Exp. – Droop FEA	4.72
Droop Exp. – Droop Target	5.26
Droop Target – Clean Target	8.10